



1 **Aerosol Responses to Precipitation Along North American Air Trajectories Arriving at**
2 **Bermuda**

3
4 Hossein Dadashazar¹, Majid Alipanah², Miguel Ricardo A. Hilario³, Ewan Crosbie^{4,5}, Simon
5 Kirschler^{6,7}, Hongyu Liu⁸, Richard H. Moore⁴, Andrew J. Peters⁹, Amy Jo Scarino^{4,5}, Michael
6 Shook⁴, K. Lee Thornhill⁴, Christiane Voigt^{6,7}, Hailong Wang¹⁰, Edward Winstead^{4,5}, Bo
7 Zhang⁸, Luke Ziemba⁴, Armin Sorooshian^{1,3}

8
9 ¹Department of Chemical and Environmental Engineering, University of Arizona, Tucson, AZ,
10 USA

11 ²Department of Systems and Industrial Engineering, University of Arizona, Tucson, AZ, USA

12 ³Department of Hydrology and Atmospheric Sciences, University of Arizona, Tucson, AZ, USA

13 ⁴NASA Langley Research Center, Hampton, VA, USA

14 ⁵Science Systems and Applications, Inc., Hampton, VA, USA

15 ⁶Institute for Atmospheric Physics, DLR, German Aerospace Center, Oberpfaffenhofen,
16 Germany

17 ⁷Institute for Atmospheric Physics, University of Mainz, Mainz, Germany

18 ⁸National Institute of Aerospace, Hampton, VA, USA

19 ⁹Bermuda Institute of Ocean Sciences, 17 Biological Station, St. George's, GE01, Bermuda

20 ¹⁰Atmospheric Sciences and Global Change Division, Pacific Northwest National Laboratory,
21 Richland, WA, USA

22

23

24 *Correspondence to: Hossein Dadashazar (hosseind@arizona.edu)

25



26 **Abstract**

27 North American pollution outflow is ubiquitous over the western North Atlantic Ocean, especially
28 in winter, making this location an ideal natural laboratory for investigating the impact of
29 precipitation on aerosol particles along air mass trajectories. We take advantage of observational
30 data collected at Bermuda to seasonally assess the sensitivity of aerosol mass concentrations and
31 volume size distributions to accumulated precipitation along trajectories (APT). The mass
32 concentration of particulate matter with aerodynamic diameter less than 2.5 μm normalized by the
33 enhancement of carbon monoxide above background ($\text{PM}_{2.5}/\Delta\text{CO}$) at Bermuda was used to
34 estimate the degree of aerosol loss during transport to Bermuda. Results for December-February
35 (DJF) show most trajectories come from North America and have the highest APTs, resulting in
36 significant reduction (by 53%) in $\text{PM}_{2.5}/\Delta\text{CO}$ under high APT conditions (> 13.5 mm) relative to
37 low APT conditions (< 0.9 mm). Moreover, $\text{PM}_{2.5}/\Delta\text{CO}$ was most sensitive to increases in APT
38 up to 5 mm ($-0.044 \mu\text{g m}^{-3} \text{ppbv}^{-1} \text{mm}^{-1}$) and less sensitive to increases in APT over 5 mm. While
39 anthropogenic $\text{PM}_{2.5}$ constituents (e.g., black carbon, sulfate, organic carbon) decrease with high
40 APT, sea salt in contrast was comparable between high and low APT conditions owing to enhanced
41 local wind and salt emissions in high APT conditions. The greater sensitivity of the fine mode
42 volume concentrations (versus coarse mode) to wet scavenging is evident from AERONET
43 volume size distribution data. A combination of GEOS-Chem model simulations of ^{210}Pb
44 submicron aerosol tracer and its gaseous precursor ^{222}Rn reveal that (i) surface aerosol particles at
45 Bermuda are most impacted by wet scavenging in winter/spring (due to large-scale precipitation)
46 with a maximum in March, whereas convective scavenging plays a substantial role in summer;
47 and (ii) North American ^{222}Rn tracer emissions contribute most to surface ^{210}Pb concentrations at
48 Bermuda in winter ($\sim 75\text{-}80\%$), indicating that air masses arriving at Bermuda experience large-
49 scale precipitation scavenging while traveling from North America. A case study flight from the
50 ACTIVATE field campaign on 22 February 2020 reveals a significant reduction in aerosol number
51 and volume concentrations during air mass transport off the U.S. East Coast associated with
52 increased cloud fraction and precipitation. These results highlight the sensitivity of remote marine
53 boundary layer aerosol characteristics to precipitation along trajectories, especially when the air
54 mass source is continental outflow from polluted regions like the U.S. East Coast.

55
56



57 **1. Introduction**

58 Aerosol properties are difficult to characterize in remote marine regions owing to the
59 scarcity of monitoring stations as compared to over land. Island observatories are critical resources
60 to investigate long-range transport of aerosol particles and their associated properties (e.g., Silva
61 et al., 2020). The western North Atlantic Ocean (WNAO) includes the island of Bermuda, which
62 has a rich history of monitoring data for both surface and columnar aerosol characteristics, thus
63 affording the opportunity to study how aerosol properties are impacted by different sources and
64 processes along the transport of air masses to the site. Consequently, Bermuda has been the subject
65 of decades of intense atmospheric science research (Sorooshian et al., 2020), especially as it is a
66 receptor site for both North African dust (Chen and Duce, 1983) and anthropogenic outflow from
67 both North America (Arimoto et al., 1992; Galloway et al., 1989; Moody et al., 2014; Corral et al.,
68 2021) and Europe (Anderson et al., 1996; Cutter, 1993). North American outflow reaching
69 Bermuda has been linked to appreciable levels of anthropogenic species (e.g., sulfate, lead,
70 elemental carbon, ozone) (Wolff et al., 1986), more acidic rainfall as compared to other air mass
71 sources (Jickells et al., 1982), and a significant reduction of sulfate levels in both aerosol and wet
72 deposition samples in response to reduced SO₂ emissions in recent decades (Keene et al., 2014).

73 There have been extensive studies reporting on some aspect of air mass history prior to
74 arrival at Bermuda (Sorooshian et al., 2020 and references therein), including predominant
75 circulation patterns impacting Bermuda at different times of the year (e.g., Miller and Harris, 1985;
76 Veron et al., 1992). What remains uncertain is how precipitation along those trajectories impacts
77 surface aerosol characteristics at Bermuda. Wet scavenging rates are very difficult to constrain
78 over open ocean areas such as the WNAO (Kadko and Prospero, 2011). Arimoto et al. (1999) used
79 aerosol radionuclide data in relation to airflow pattern information to conclude that pollutant
80 transport to Bermuda is common from the northwest and that precipitation scavenging can be
81 influential; their analysis of rain effects on nuclide activities were based on rain data collected at
82 Bermuda without knowledge of rain along trajectory pathways. While many studies have
83 investigated how composition at Bermuda varies based on air mass trajectories, the subject of how
84 precipitation along those trajectories impact the resultant aerosol at Bermuda has not been
85 adequately addressed but is motivated by past works (Moody and Galloway, 1988; Todd et al.,
86 2003).

87 In their recent aerosol climatology study for Bermuda, Aldhaif et al. (2021) found the
88 peculiar result that fine particulate pollution in the winter months (December-February) was
89 reduced even though there was an enhanced number density of air mass back trajectories traced
90 back to North America. They hypothesized that enhanced seasonal cloud fractions and
91 precipitation in winter (Painemal et al., 2021) contribute to the removal of aerosol particles during
92 transport via wet scavenging, which we aim to study more deeply here using a variety of datasets.
93 Results of this study have broad relevance to all remote marine regions impacted by transported
94 continental pollution, in addition to advancing knowledge of how precipitation can impact surface
95 aerosol characteristics.

96
97 **2. Datasets and Methods**

98 Datasets used in this work are summarized in Table 1 and described in brief detail below.
99

100
101
102



103
 104
 105
 106
 107
 108
 109
 110

Table 1. Summary of datasets used in this work. Data are between 1 January 2015 and 31 December 2019, with the exception of ACTIVATE aircraft data based on a single flight day on 22 February 2020. GEOS-Chem simulations are separately described in Section 2.5. Section 2 provides more details about the datasets used in this study, including specific instruments from the ACTIVATE airborne dataset.

Parameter	Acronym	Data Source	Time Resolution	Website
Particulate matter mass concentration (aerodynamic diameter less than 2.5 μm)	PM _{2.5}	Fort Prospect Station	Hourly	https://doi.org/10.6084/m9.figshare.13651454.v2
Particulate matter mass concentration (aerodynamic diameter less than 10 μm)	PM ₁₀	Fort Prospect Station	Daily	https://doi.org/10.6084/m9.figshare.13651454.v2
Nitrogen monoxide concentration	NO	Fort Prospect Station	Hourly	https://doi.org/10.6084/m9.figshare.13651454.v2
Nitrogen dioxide concentration	NO ₂	Fort Prospect Station	Hourly	https://doi.org/10.6084/m9.figshare.13651454.v2
Nitrogen oxide concentration	NO _x	Fort Prospect Station	Hourly	https://doi.org/10.6084/m9.figshare.13651454.v2
Volume size distribution	VSD	AERONET	Hourly	https://aeronet.gsfc.nasa.gov/
Carbon monoxide surface concentration	CO	MERRA-2	Hourly	https://disc.gsfc.nasa.gov/
Aerosol speciated surface mass concentrations	-	MERRA-2	Hourly	https://disc.gsfc.nasa.gov/
Surface wind speed	WindsF	MERRA-2	Hourly	https://disc.gsfc.nasa.gov/
Planetary boundary layer height	PBLH	MERRA-2	Hourly	https://disc.gsfc.nasa.gov/
Back-trajectory	-	HYSPLIT	N/A	https://www.ready.noaa.gov/HYSPLIT.php
Precipitation	APT/Rain	GDAS	Hourly	https://www.ready.noaa.gov/archives.php
Aerosol/cloud properties	-	Airborne: ACTIVATE	1 – 45 Sec	https://doi.org/10.5067/SUBORBITAL/ACTIVATE/DATA001

111
 112
 113

2.1 Bermuda Surface Measurements

Aerosol and gas measurements were conducted at Fort Prospect in Bermuda (32.30° N, 64.77°W, 63 m ASL). Hourly PM_{2.5} data were collected with a Thermo Scientific TEOM 1400a Ambient Particulate Monitor with 8500C FDMS (Federal Equivalent Method EQPM-0609-181 for PM_{2.5}). Concentrations were determined by employing conditioned filter sample collection and direct mass measurements using an inertial micro-balance (TEOM 1400a). Hourly precision was $\pm 1.5 \mu\text{g m}^{-3}$. Hourly data were averaged every 6 hours to match the time frequency of the trajectory analysis discussed subsequently.

PM₁₀ concentrations were determined based on U.S. Environmental Protection Agency (EPA) method IO-2 (EPA, 1999) using a Tisch model TE6070 hi-volume air sampler, equipped with 8" \times 10" TissuQuartz 2500 QAT-UP quartz fiber filters. The PM₁₀ sampler was operated at a flow rate of 2.1 m³ min⁻¹ yielding a total volume of 3000 m³ over a 24 hr sampling period. The sampler flow rate was calibrated every 3 months. Sampling was synchronized with the 1-in-6 day national ambient air quality schedule used by EPA. Prior to deployment, the filters were equilibrated for 24 hr in an environmental control chamber maintaining constant conditions of relative humidity (35 \pm 2%) and temperature (21 \pm 2°C). The filters were then weighed with a precision of ± 0.1 mg using a Mettler Toledo AB104 balance, which was modified for weighing unfolded 8" \times 10" filters, and then transferred to clean re-sealable plastic bags for transportation to the field site. After sampling, the exposed filters were returned immediately to the laboratory where they were re-equilibrated in the environmental control chamber for 24 hr before being re-weighed



134 to determine the particle loading from which particle concentrations were calculated. PM₁₀
135 determinations have an accuracy of within $\pm 2.5\%$, which is equivalent to $\pm 0.2 \mu\text{g m}^{-3}$ based on
136 the average of PM_{2.5} between 2015 and 2019 (i.e., $6.7 \mu\text{g m}^{-3}$).

137 Various gases were monitored with hourly time resolution using a Model T200U Trace-
138 level NO/NO₂/NO_x analyzer (Teledyne API), which is a U.S. EPA compliance analyzer relying on
139 a proven chemiluminescence principle. The gas analyzer was routinely calibrated using NIST-
140 certified calibrant NO₂ in ultra-high purity nitrogen (Airgas, Inc., Radnor Township, PA, USA).
141 Acceptable criteria applied for single point quality control (QC) allows for $\pm 15.1\%$ or $< \pm 1.5$ ppb
142 difference, whichever is greater (40 CFR Part 58 App A Sec. 3.1.1). Similar to PM_{2.5}, these hourly
143 gas data were averaged to 6-hour resolution.

144 Columnar aerosol data were obtained from a NASA AErosol RObotic NETwork
145 (AERONET) (Holben et al., 1998) surface station at Tudor Hill (32.264° N, 64.879° W). Level 2
146 daily data have been quality assured and cloud screened based on the Version 3 algorithm (Giles
147 et al., 2019). We focus on the volume size distribution (VSD) product that has 22 logarithmically
148 equidistant discrete radii ranging from 0.05 to 15 μm . A radius of 0.6 μm typically discriminates
149 between fine and coarse modes when using AERONET data (Dubovik et al., 2002; Schuster et al.,
150 2006).

151

152 **2.2 Reanalysis Data**

153 Modern-Era Retrospective analysis for Research and Applications-Version 2 (MERRA-2)
154 (Gelaro et al., 2017) products were used as a data source for speciated aerosol and gas parameters
155 including surface mass concentration of sea-salt (collection “avg1_2d_aer_Nx”) and surface
156 concentration of carbon monoxide (CO; collection “avg1_2d_chm_Nx”). Surface wind speed and
157 planetary boundary layer height (PBLH) (collection “avg1_2d_flux_Nx”) data were also obtained
158 from MERRA-2. Hourly and 3-hourly data were downloaded and averaged for a 0.5° latitude by
159 0.625° longitude grid (i.e., 32° – 32.5°N and 64.375° – 65°W) surrounding Bermuda and
160 subsequently converted to 6-hour data to match the time frequency of trajectory analysis results.

161

162 **2.3 Air Mass Trajectory Analysis**

163 To track air mass pathways arriving at Bermuda (32.30° N, 64.77°W), we obtained 10-day
164 (240 hr) back-trajectories from the Hybrid Single-Particle Lagrangian Integrated Trajectory model
165 (HYSPLIT) (Stein et al., 2015; Rolph et al., 2017). We used an ending altitude of 100 m (AGL) to
166 be within the surface layer and close to the measurement site. As discussed later, sensitivity
167 analysis with higher ending altitudes (500 m and 1 km; Figs. S1-S2) reveal similar results to using
168 100 m. Four trajectories were initialized (i.e., 6-hour interval) each day between 1 January 2015
169 00:00:00 UTC and 31 December 2019 18:00:00 UTC resulting in a total of 7304 individual
170 trajectories. Trajectories were calculated using the Global Data Assimilation System (GDAS) one-
171 degree archive data and with the “model vertical velocity” method, which is a way that vertical
172 motion is handled in HYSPLIT for trajectory calculations. Precipitation data were also obtained
173 along the trajectories based on GDAS one-degree data. Results presented in Figs. 1-3 are based on
174 10-day back-trajectories, whereas analyses presented in the remaining sections of the paper are
175 based on 4-day (96 hr) back-trajectories.

176

177 **2.3.1 Concentration Weighted Trajectory Analysis and Seasonal Rain Maps**

178 Concentration weighted trajectories (CWT) were calculated based on the 10-day back-
179 trajectories from HYSPLIT in conjunction with Bermuda surface PM_{2.5} data described in Section



180 2.1. The CWT method has been implemented widely to identify long-range pollutant transport
181 pathways impacting a receptor site (Hsu et al., 2003; Wang et al., 2009; Hilario et al., 2020).
182 Seasonal maps of average precipitation experienced by trajectories were also estimated based on
183 10-day back-trajectories from HYSPLIT. The aforementioned analyses were performed for
184 $0.5^\circ \times 0.5^\circ$ grids covering the area encompassed by 10° – 80° N and 5° – 170° W. A weight function
185 following the method of Dimitriou et al. (2015) was applied in the CWT analysis and precipitation
186 maps to increase statistical stability.

187

188 **2.3.2 Trajectory Clustering**

189 Hierarchical agglomerative clustering was used to identify characteristic trajectories
190 reaching Bermuda at 100 m (AGL). Hierarchical clustering was based on the “complete linkage”
191 method (Govender and Sivakumar, 2020). Four-day HYSPLIT back-trajectories were used to
192 perform clustering analysis. Distances between trajectories were calculated using the Haversine
193 formula, which calculates distance between two points on Earth assuming they are on a great circle
194 (Sinnott, 1984). Clustering was performed for varying numbers of clusters, ranging between 2 and
195 32. The L-method (Kassomenos et al., 2010) was implemented to identify the optimum number of
196 clusters. In this method, root mean square deviation (RMSD) was calculated for each clustering
197 run and then plotted versus the number of clusters to determine the optimum solution. RMSDs
198 were estimated based on the distances between trajectories and associated mean cluster
199 trajectories.

200

201 **2.4 Airborne Measurements**

202 Airborne data from the Aerosol Cloud meteorology Interactions oVer the western ATLantic
203 Experiment (ACTIVATE) are used from Research Flight 6 (RF6) on 22 February 2020.
204 ACTIVATE involves two NASA Langley aircraft (HU-25 Falcon and UC-12 King Air) flying in
205 coordination at different altitudes to simultaneously characterize the same vertical column with a
206 focus on aerosol-cloud-meteorology interactions (Sorooshian et al., 2019). RF6 was a rare case of
207 the HU-25 Falcon flying alone, but this aircraft conveniently included measurements relevant to
208 this study. The ACTIVATE strategy involves the HU-25 Falcon flying in the boundary layer to
209 characterize gas, aerosol, cloud, and meteorological parameters along the following level legs:
210 Min. Alt. = lowest altitude flown (500 ft), BCB = below cloud base, ACB = above cloud base,
211 BCT = below cloud top, ACT = above cloud top.

212 Data from the following instruments were used: Condensation Particle Counter (CPC; TSI
213 Model 3772) for number concentration of particles with diameter > 10 nm; Scanning Mobility
214 Particle Sizer (SMPS; TSI Model 3081) for aerosol size distribution data between 3.2 – 89.1 nm;
215 Laser Aerosol Spectrometer (LAS; TSI Model 3340) for aerosol size distribution data between
216 diameters of 0.09 – 5 μ m; two-dimensional optical array imaging probe (2DS; SPEC Inc.) (Lawson
217 et al., 2006) for rain water content (RWC) quantified by integrating rain drop size distributions
218 between diameters of 39.9 – 1464.9 μ m; and Fast Cloud Droplet Probe (FCDP; SPEC Inc.) (Knop
219 et al., 2021) for cloud liquid water content (LWC) calculated by integrating drop size distributions
220 between diameters of 3 – 50 μ m. With the exception of SMPS data (45 second resolution), all
221 airborne data were at 1 second resolution.

222

223 **2.5 Radionuclide tracers in GEOS-Chem Model**

224 Lead-210 (^{210}Pb , half-life 22.3 years) is the decay daughter of ^{222}Rn (half-life 3.8 days)
225 emitted mainly from land surfaces. After production, it indiscriminately attaches to ambient



226 submicron particles, which move with the air until being scavenged by precipitation or deposited
227 to the surface. Because of its relatively well-known source and wet deposition as its principal sink,
228 ^{210}Pb has long been used to test wet deposition processes in global models (e.g., Liu et al., 2001).
229 It is also a useful tracer to describe continental air influence over oceans. In this study, we use
230 ^{210}Pb as simulated by the GOES-Chem model to investigate the role of precipitation scavenging
231 in affecting seasonal surface aerosol concentrations at Bermuda.

232 GEOS-Chem (<http://www.geos-chem.org>) is a global 3-D chemical transport model driven
233 by meteorological fields from the Goddard Earth Observing System (GEOS) of the NASA Global
234 Modeling and Assimilation Office (Bey et al., 2001; Eastham et al., 2014). It has been widely used
235 to study trace gases and aerosols in the atmosphere. Here we use the model version 11-01
236 (http://wiki.seas.harvard.edu/geos-chem/index.php/GEOS-Chem_v11-01) driven by the MERRA-
237 2 reanalysis (at 2.5° longitude by 2° latitude resolution) to simulate ^{222}Rn and ^{210}Pb . The model
238 simulates the emission, transport (advection, convection, boundary layer mixing), deposition, and
239 decay of the radionuclide tracers (Liu et al., 2001; Brattich et al., 2017; Yu et al., 2018; Zhang et
240 al., 2021). As a function of latitude, longitude, and month, ^{222}Rn emission uses a customized
241 emission scenario that was built upon previous estimates and evaluated against global ^{222}Rn
242 surface observations and vertical profile measurements (Zhang et al., 2021). GEOS-Chem uses the
243 TPCORE advection algorithm of Lin and Rood (1996), calculates convective transport using
244 archived convective mass fluxes (Wu et al., 2007), and uses the non-local boundary-layer mixing
245 scheme implemented by Lin and McElroy (2010). The wet deposition scheme follows that of Liu
246 et al. (2001) and includes rainout (in-cloud scavenging) due to large-scale (stratiform and anvil)
247 precipitation, scavenging in convective updrafts, and washout (below-cloud scavenging) by
248 precipitation (Wang et al., 2011). A modification to the large-scale precipitation scavenging
249 scheme is included to use spatiotemporally varying cloud water contents from MERRA-2 instead
250 of a fixed constant value in the original model (Luo et al., 2019). Dry deposition is based on the
251 resistance-in-series scheme of Wesely (1989).

252

253 **3. Results and Discussion**

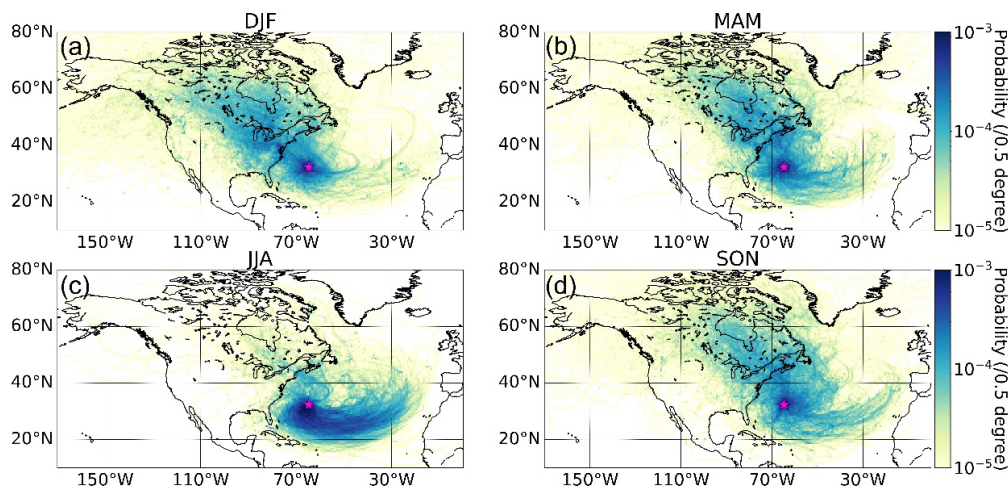
254 **3.1 Seasonal Profiles**

255 **3.1.1 Back-Trajectories**

256 Our results in Fig. 1 show that the summer months (June-August, JJA) are distinct due to
257 the Bermuda High promoting easterly winds at latitudes south of Bermuda that turn north and
258 become southwesterly (\sim parallel to U.S. East Coast) towards Bermuda. The Bermuda high
259 pressure system and its associated anticyclonic circulation in the boundary layer have been
260 reported to be strongest in April–September (Merrill, 1994; Moody et al., 1995). This high pressure
261 system breaks down in other months in favor of strengthened extratropical subpolar low pressure,
262 thus yielding more air influence from the northwest and west (Arimoto et al., 1995; Davis et al.,
263 1997), which is clearly evident in the other three seasonal panels of Fig. 1 and most pronounced
264 in the winter months (December-February, DJF). In their analysis of air mass history leading to
265 rain events over Bermuda, Altieri et al. (2013) observed more influence from air originating over
266 water in warmer months (April–September) and faster moving air masses originating over the
267 continental U.S. primarily in the colder months of October–March. Moody and Galloway (1988)
268 also showed that cool months (October–March) were marked by more transport from the U.S. East
269 Coast. It can be deduced from Fig. 1 that based on the farther reaching source areas of the back-
270 trajectories in colder months, and especially DJF, that air moves faster in the boreal winter. Finally,
271 we note that Figs. S1-S2 show the same results as Fig. 1 but with ending altitudes of 500 m and 1



272 km over Bermuda; the sensitivity tests indicate the same general results and thus we continue the
273 discussion using results based on 100 m.



274
275 **Figure 1. Seasonal maps (a-d) showing the probability density of trajectories calculated**
276 **based on 10-day HYSPLIT backward trajectories reaching Bermuda (32.30° N, 64.77°W),**
277 **denoted by the pink star, at 100 m (AGL). This analysis is based on trajectories between 01**
278 **January 2015 and 31 December 2019. Analogous results for ending altitudes of 500 m and 1**
279 **km are shown in Figs. S1 and S2, respectively.**

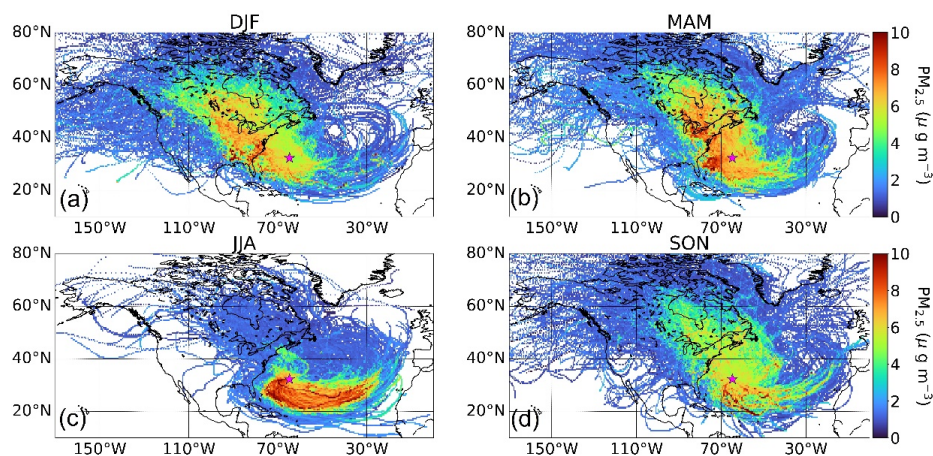
280 281 3.1.2 Surface Aerosol and NO_x

282 Recent work has shown a seasonal cycle over Bermuda for column-integrated aerosol
283 properties, with aerosol optical depth (AOD) being highest in March-May (MAM) and
284 lowest in September-November (SON) and DJF (Aldhaif et al., 2021). They further showed that
285 sea salt contributed more to AOD in the colder months (SON, DJF) whereas sulfate, organic
286 carbon, black carbon and dust were more dominant in MAM and JJA. In their examination of
287 aerosol type seasonality at Bermuda, Huang et al. (1999) observed that marine and crustal elements
288 peaked in winter and summer, respectively, and that pollution-derived particles dominated in
289 spring with a smaller peak in fall. We use Fort Prospect data to gain a revised perspective about
290 seasonality and the weekly cycle of surface layer aerosol and additionally NO_x (box notch plots in
291 Figs. S3a-f).

292 Median seasonal concentrations of PM_{2.5} ($\mu\text{g m}^{-3}$) were as follows at Bermuda, being
293 largely consistent with the AOD seasonal cycle: DJF = 5.50, MAM = 6.36, JJA = 6.11, SON =
294 5.33 (Fig. S3). NO_x exhibited a similar seasonal pattern (ppbv): DJF = 17.76, MAM = 21.62, JJA
295 = 18.68, SON = 13.95 (Fig. S3). It is difficult to ascertain sources and impacts of precipitation on
296 PM_{2.5} based on these values. As a next step we present the seasonal CWT maps showing the
297 predominant pathways accounting for the majority of PM_{2.5} at Bermuda (Fig. 2). Expectedly, PM_{2.5}
298 in JJA is largely accounted for by trajectories following the general anticyclonic circulation already
299 shown in Fig. 1c associated with the Bermuda High. These air masses are enriched with African
300 dust as has been documented in many past studies (e.g., Arimoto, 2001; Huang et al., 1999; Muhs



301 et al., 2012). In contrast, the other seasons (especially DJF and MAM) showed greater relative
302 influence from North American outflow versus other source regions.



303 **Figure 2. Seasonal (a-d) concentration-weighted trajectory maps (CWT) for PM_{2.5} measured**
304 **at Fort Prospect in Bermuda, denoted by the pink star. This analysis is based on trajectories**
305 **between 1 January 2015 and 31 December 2019.**
306
307

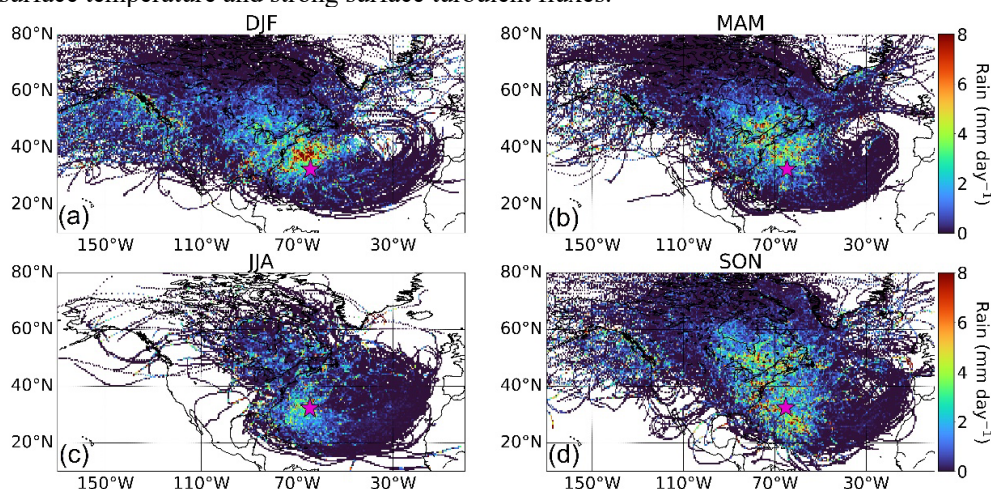
308 While we focus on long-range transport of PM_{2.5} to Bermuda, local sources cannot be
309 ignored, including both sea salt and non-sea salt species (e.g., Galloway et al., 1988). The island
310 has a population of approximately 64,000 as of 2016 (Government of Bermuda, 2019). Local
311 influence from anthropogenic sources has been reported to be insignificant in contrast to
312 transported pollution (Galloway et al., 1988; Keene et al., 2014). We assess how significant local
313 anthropogenic sources are based on day-of-week aerosol concentrations and whether significantly
314 higher levels exist on working days as compared to weekend days as shown in other regions with
315 strong anthropogenic influence (Hilario et al., 2020 and references therein). Our analysis found
316 negligible difference between working days (Monday-Friday) and weekend days (Saturday-
317 Sunday) for both PM_{2.5} and NO_x (Figs. S3b/d), including when resolved by season (Figs. S4-S5).
318 Therefore, it is less likely that local anthropogenic emissions dominate the island's PM_{2.5} and NO_x,
319 providing support for transported sources being more influential; as will be shown, normalizing
320 PM_{2.5} by CO helps control for local anthropogenic influence.

321 We also examined seasonal and day-of-week statistics for PM₁₀ to assess the relative
322 importance of coarse aerosol types including mainly sea salt and dust (Figs. S3e-f). Results reveal
323 the highest median PM₁₀ values ($\mu\text{g m}^{-3}$) in DJF (19.24), followed by MAM (18.51), JJA (17.98),
324 and SON (15.88). As will be shown later and already documented (Aldhaif et al., 2021), surface
325 wind speeds around Bermuda are highest in DJF, contributing to higher sea salt emissions.
326 Expectedly there was no observable PM₁₀ weekly cycle as dust and sea salt are naturally emitted.
327 Both PM_{2.5} and PM₁₀ exhibited their highest seasonal standard deviations in JJA owing most likely
328 to the episodic nature of some pollution events such as with dust and biomass burning (e.g., Aldhaif
329 et al., 2021).
330



331 3.1.3 Precipitation Along Trajectories

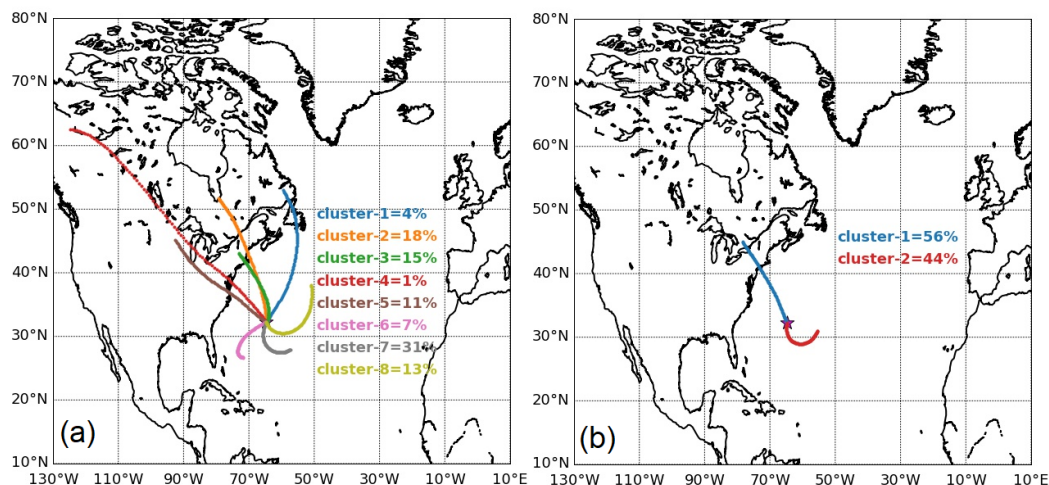
332 Figure 3 shows seasonal profiles of average precipitation rate obtained from GDAS (Table
333 1) in $0.5^\circ \times 0.5^\circ$ grids based on 10-day back trajectories arriving at Bermuda (100 m AGL). The
334 spatiotemporal pattern of precipitation over the WNAO is of most interest in terms of potential
335 impacts on wet scavenging of aerosol during the transport of North American pollution to
336 Bermuda. In that regard, DJF shows the most pronounced levels of precipitation to the north and
337 northwest of Bermuda over the WNAO, coincident with strong and frequent convection linked to
338 frontogenesis (Painemal et al., 2021). This is consistent with how Painemal et al. (2021) showed
339 that precipitation exhibits maximum levels over the Gulf Stream path owing to relatively high sea
340 surface temperature and strong surface turbulent fluxes.



341 **Figure 3. Seasonal maps (a-d) of average precipitation occurring in $0.5^\circ \times 0.5^\circ$ grids based on**
342 **10-day backward trajectories reaching Bermuda (32.30° N, 64.77° W; pink star) at 100 m**
343 **(AGL). This analysis is based on trajectories between 1 January 2015 and 31 December 2019.**
344
345

346 3.2 Trajectory Clustering

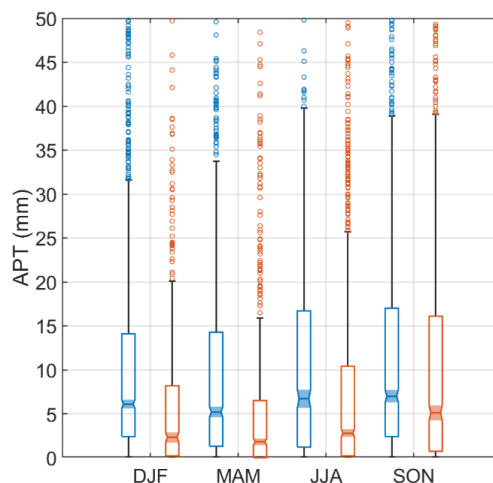
347 Prior to examining how precipitation directly impacts $PM_{2.5}$ at Bermuda, we identify
348 characteristic trajectory pathways using the hierarchical agglomerative clustering method
349 described in Section 2.3.2. We reiterate that this analysis is based on 4 days of back-trajectories,
350 rather than 10 days from Figs. 1-3, to focus more on transport closer to Bermuda. The optimum
351 solution based on the L-method (see Section 2.3.2) resulted in eight trajectory clusters (Fig. 4a),
352 with five (numbered 1-5) coming from North America and the remaining three (numbered 6-8)
353 more characteristic of the anticyclonic circulation described already for JJA. The former five
354 clusters account for 49% of the total trajectories, with the latter three responsible for the remaining
355 51%. The majority of trajectories from North America come offshore north of North Carolina (i.e.,
356 coastal areas north of $\sim 35^\circ$ N).



357
358 **Figure 4. Cluster mean trajectories based on the (a) optimum solution having eight clusters**
359 **and (b) a simplified solution with two clusters to enhance statistics for North American**
360 **trajectories. Clustering was performed on four-day HYSPLIT backward trajectories**
361 **between 1 January 2015 and 31 December 2019.**
362

363 For the sake of simplicity of the remainder of the discussion, we reduced the number of
364 characteristic trajectories to two (Fig. 4b) to have one from North America and the other from the
365 southeast. Using only two clusters increases the number of data points in the North American
366 cluster for more robust calculations of rain-aerosol relationships. Our choice to put together all
367 North American air mass clusters into one group is aligned with a similar clustering choice by
368 Chen and Duce (1983; see their Fig. 3) where trajectories were grouped together from Florida to
369 the Canadian maritime provinces. Also, Mead et al. (2013) divided trajectory data ending at
370 Bermuda into “Saharan” and “non-Saharan” seasons that generally coincide with our division of
371 data into two clusters. Cluster 1 from North America accounts for 56% of trajectories and Cluster
372 2 from the southeast is linked to 44% of trajectories. It is clear from the two clusters that the North
373 American air masses generally move faster as the characteristic 4-day back-trajectories originate
374 farther away from Bermuda than that of Cluster 2.

375 Regardless of season, Cluster 1 was associated with higher APT values with the seasonal
376 median values (units of mm) as follows (Cluster1/Cluster 2): DJF = 6.1/2.3; MAM = 5.2/1.8; JJA
377 = 6.7/2.8; SON = 7.0/5.1. Figure 5 shows a box notch plot comparing APT between clusters for
378 each season, demonstrating statistically significant differences in median values between clusters
379 for a given season at 95% confidence. Furthermore, Cluster 1 exhibited higher CO levels at
380 Bermuda for each season with median values (units of ppbv) as follows (Cluster 1/Cluster 2): DJF
381 = 89.7/76.3; MAM = 88.5/75.0; JJA = 68.9/58.7; SON = 81.6/65.6. Therefore, the combination of
382 pollution outflow from North America and higher APT values makes Cluster 1 more ideal in terms
383 of identifying potential wet scavenging effects on transported aerosol over the WNAO. The
384 remainder of the study thus focuses on Cluster 1.



385
386 **Figure 5. Box notch plot for each season comparing accumulated precipitation along**
387 **trajectories (APT) for Clusters 1 (blue) and 2 (orange) from Fig. 4b. APT values were**
388 **estimated from four-day HYSPLIT back trajectories reaching Bermuda (32.30° N, 64.77°W)**
389 **at 100 m AGL. The middle, bottom, and top lines in each box represent the median, 25th**
390 **percentile, and 75th percentile, respectively. Markers show extreme values identified based**
391 **on 1.5×IQR (interquartile range) distance from the top of each box. Whiskers represent**
392 **maximum and minimum values excluding extreme points. Boxes with notches and shaded**
393 **regions that do not overlap have different medians at the 95% confidence level.**
394

395 3.3 North America Trajectory Results

396 We next examine the relationship between APT and aerosol transport to Bermuda based
397 on Cluster 1 results (Table 2). We compare data for “low” and “high” APT values based on
398 thresholds being the 25th percentile (< 0.9 mm) and 75th percentile (> 13.5 mm), respectively, based
399 on cumulative data from all seasons and years. As wet scavenging is expected to reduce PM_{2.5}
400 during its transport from North America to Bermuda, we anticipate lower PM_{2.5} values at high
401 APT. However, the results indicate this is only the case for MAM and JJA, with similar median
402 values in SON and a higher median value in DJF for high APT conditions. Interestingly, NO, NO₂,
403 NO_x, and CO were all significantly higher in DJF for high APT conditions too, raising the issue
404 that absolute concentrations should be normalized to account for the differences in concentration
405 that existed closer to North America prior to potential wet scavenging over the WNAO.

406 CO exhibits three important traits qualifying it as a species to normalize PM_{2.5} by: (i) a
407 reliable marker of anthropogenic pollution stemming from North America (Corral et al., 2021);
408 (ii) being relatively insensitive to wet scavenging processes; and (iii) having a long lifetime in the
409 atmosphere (~1 month; Weinstock, 1969) compared to aerosol particles. Consequently, we
410 normalize PM_{2.5} by ΔCO to quantify transport efficiency and to reveal the potential effects of wet
411 scavenging as has been done in past studies for other regions (Park et al., 2005; Garrett et al., 2010;
412 Hilario et al., 2021; Matsui et al., 2011; Moteki et al., 2012; Oshima et al., 2012). We first
413 determine the 5th percentile value of surface CO at Bermuda for each season for Cluster 1
414 trajectories and assume those are the seasonal background values as done also by Matsui et al.



415 (2011). We then calculate ΔCO as the difference between each 6-hourly CO data point at Bermuda
416 and the background value for a given season. We only use data when $\Delta\text{CO} > 3.2$ ppbv to ensure a
417 sufficiently high signal to noise ratio (Garrett et al., 2010).

418

419 **Table 2. Seasonal medians of aerosol, gas, and meteorological variables for Cluster 1 divided**
420 **into high- and low-APT categories. Differences in median values that are statistically**
421 **significant (p-value < 0.05) based on a Wilcoxon rank-sum test are highlighted with bold and**
422 **italic font. Percentage differences* between high- and low-APT median values are provided**
423 **in parentheses. NO, NO₂, NO_x, and PM_{2.5} are based on Fort Prospect measurements, whereas**
424 **all other parameters are from MERRA-2 with the exception of the two APT rows (derived**
425 **from HYSPLIT and GDAS) and the last 8 rows corresponding to AERONET volume size**
426 **distribution data. We combined all seasons for AERONET data to have sufficient statistics**
427 **for comparisons (high APT = 16 points, low APT = 19 points). AERONET parameters**
428 **include volume concentration (V), effective radii (R_{eff}), volume median radii (R), and**
429 **geometric standard deviation (σ) with subscripts f and c for fine and coarse modes,**
430 **respectively. Number of data points for each table entry is summarized in Table S1.**

431



432

Parameter	High-rain (APT > 13.5 mm)/Low-rain (APT < 0.9 mm) (% Difference [*])			
	DJF	MAM	JJA	SON
NO (ppbv)	6.0/3.5 (71 %)	7.3/7.8 (-6 %)	8.3/13.1 (-37 %)	3.8/4.2 (-10 %)
NO ₂ (ppbv)	13.9/12.8 (9 %)	13.4/12.0 (12 %)	8.6/6.6 (30 %)	9.4/9.2 (2 %)
NO _x (ppbv)	19.6/17.5 (12 %)	21.2/21.8 (-3 %)	17.4/23.3 (-25 %)	14.1/14.2 (-1 %)
CO (ppbv)	97.8/84.7 (15 %)	92.4/88.6 (4 %)	70.8/65.9 (7 %)	83.7/81.4 (3 %)
PM _{2.5} (µg m ⁻³)	6.1/5.5 (11 %)	6.7/7.3 (-8 %)	5.9/7.8 (-24 %)	5.5/5.1 (8 %)
PM _{2.5} /ΔCO (µg m ⁻³ ppbv ⁻¹)	0.29/0.62 (-53 %)	0.35/0.51 (-31 %)	0.32/0.37 (-14 %)	0.27/0.33 (-18 %)
Sea-Salt (µg m ⁻³)	47.2/28.4 (66 %)	44.1/25.4 (74 %)	27.0/26.0 (4 %)	50.6/36.0 (41 %)
Sea-Salt _{PM2.5} (µg m ⁻³)	6.2/4.0 (55 %)	6.2/4.1 (51 %)	4.9/4.9 (0 %)	6.8/5.0 (36 %)
Dust (µg m ⁻³)	0.80/0.91 (-12 %)	2.32/3.03 (-23 %)	4.47/3.02 (48 %)	1.16/1.04 (12 %)
Dust _{PM2.5} (µg m ⁻³)	0.31/0.34 (-9 %)	0.79/1.00 (-21 %)	1.58/1.18 (34 %)	0.44/0.36 (22 %)
Sea-Salt/ΔCO (µg m ⁻³ ppbv ⁻¹)	2.10/2.74 (-23 %)	2.54/1.70 (49 %)	1.50/1.58 (-5 %)	2.44/1.66 (47 %)
Sulfate/ΔCO (µg m ⁻³ ppbv ⁻¹)	0.029/0.055 (-47 %)	0.041/0.052 (-21 %)	0.039/0.046 (-15 %)	0.024/0.027 (-11 %)
Dust/ΔCO (µg m ⁻³ ppbv ⁻¹)	0.038/0.082 (-54 %)	0.129/0.186 (-31 %)	0.235/0.152 (55 %)	0.052/0.047 (11 %)
BC/ΔCO (µg m ⁻³ ppbv ⁻¹)	0.0031/0.0056 (-45 %)	0.0042/0.0057 (-26 %)	0.0041/0.0049 (-16 %)	0.0032/0.0033 (-3 %)
OC/ΔCO (µg m ⁻³ ppbv ⁻¹)	0.0093/0.0238 (-61 %)	0.0164/0.0276 (-41 %)	0.0225/0.0287 (-22 %)	0.0127/0.0153 (-17 %)
Sea-Salt _{PM2.5} /ΔCO (µg m ⁻³ ppbv ⁻¹)	0.263/0.403 (-35 %)	0.352/0.262 (34 %)	0.284/0.298 (-5 %)	0.331/0.255 (30 %)
Dust _{PM2.5} /ΔCO (µg m ⁻³ ppbv ⁻¹)	0.015/0.033 (-55 %)	0.042/0.062 (-32 %)	0.087/0.053 (64 %)	0.018/0.017 (6 %)
Wind _{SP} (m s ⁻¹)	8.5/7.1 (20 %)	8.4/5.9 (42 %)	4.4/4.7 (-6 %)	7.7/6.6 (17 %)
APT _{6h} (mm)	0.1/0.0 (NaN)	0.0/0.0 (NaN)	0.0/0.0 (NaN)	0.0/0.0 (NaN)
APT (mm)	24.7/0.0 (NaN)	22.6/0.2 (11200 %)	24.1/0.0 (NaN)	25.0/0.2 (12400 %)
All				
V _f /ΔCO × 10 ⁴ (µm ³ µm ⁻² ppbv ⁻¹)	3.42/7.55 (-55 %)			
R _{eff-r} (µm)	0.158/0.147 (7 %)			
R _r (µm)	0.176/0.171 (3 %)			
σ _r	0.471/0.470 (0 %)			
V _c /ΔCO × 10 ⁴ (µm ³ µm ⁻² ppbv ⁻¹)	2.04/2.12 (-4 %)			
R _{eff-c} (µm)	1.956/2.085 (-6 %)			
R _c (µm)	2.503/2.562 (-2 %)			
σ _c	0.684/0.647 (6 %)			

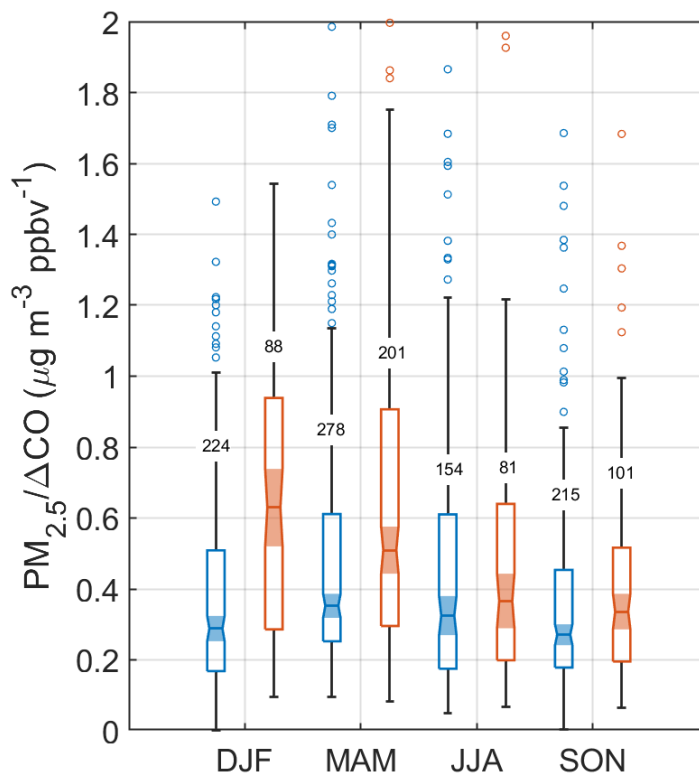
433

434
$$*\% \text{ difference} = \frac{X_{\text{High-rain}} - X_{\text{Low-rain}}}{X_{\text{Low-rain}}} \times 100$$



435
436
437
438
439
440
441
442
443
444
445
446
447
448
449
450
451

With the normalization technique, $PM_{2.5}/\Delta CO$ exhibits lower values in the high APT category for each season as compared to low APT conditions (Fig. 6), with differences between medians being statistically significant in DJF and MAM based on p-value < 0.05 with a Wilcoxon rank-sum test (Table 2). The DJF season exhibits the greatest reduction of this ratio (by 53%) in high APT conditions ($0.29 \mu g m^{-3} ppbv^{-1}$ versus $0.62 \mu g m^{-3} ppbv^{-1}$ based on median values; Table 2). Therefore, these results suggest that it is plausible that wet scavenging has a marked impact on surface $PM_{2.5}$ at a remote ocean site in the WNAO. This also helps support the speculation proposed by Aldhaif et al. (2021) that wet scavenging can reconcile why, in particular for DJF, the high density of trajectories coming from North America correlates with a reduction in fine particulate pollution arriving at Bermuda as compared to other seasons. It is noteworthy that the highest median value of $PM_{2.5}/\Delta CO$ was for the low APT category of DJF providing support for how that season has both greater influence of aerosol transport from North America (when the precipitation scavenging potential is reduced during low APT periods) and the greatest sensitivity to the effects of precipitation over the WNAO owing to the widest range in this ratio's value between high and low APT categories.

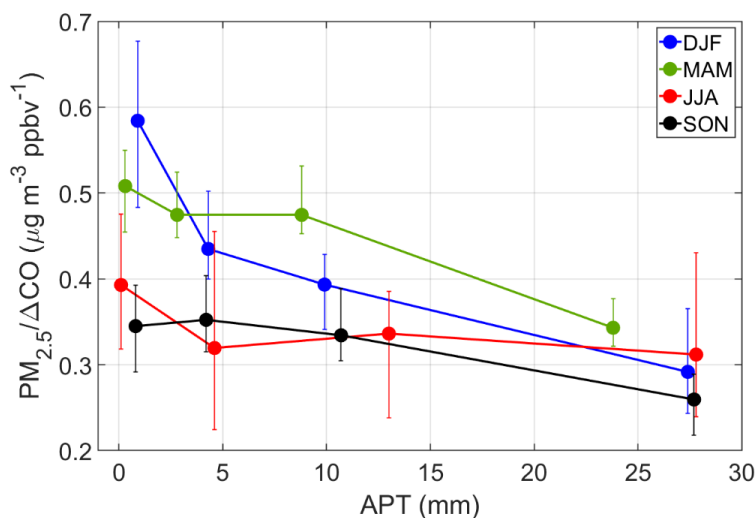


452
453
454
455
456
457

Figure 6. Box notch plot for each season comparing the $PM_{2.5}/\Delta CO$ ratio for Cluster 1 trajectories for high-APT (blue) and low-APT (orange) conditions. APT thresholds are based on 25th (< 0.9 mm) and 75th (> 13.5 mm) percentiles of APT for all trajectories reaching Bermuda between 1 January 2015 and 31 December 2019. The number of samples in each group is placed on whiskers.



458 Figure 7 additionally shows the seasonal sensitivity of $PM_{2.5}/\Delta CO$ to APT based on four
459 bins of APT chosen in such a way to provide similar numbers of data points per bin for each
460 particular season. DJF and MAM show the greatest reductions from the first to last bin as expected
461 based on Table 2, but these also were the only two seasons showing reductions between each
462 successive bin. In contrast, SON and JJA exhibited more variable behavior with $PM_{2.5}/\Delta CO$
463 actually increasing between a pair of bins in each season. A number of reasons can potentially
464 explain the less pronounced reduction in $PM_{2.5}/\Delta CO$ for SON and JJA: (i) lower values to begin
465 with in the lowest APT bins (and thus lower potential for scavenging to occur); (ii) potential
466 humidity effects associated with air masses at higher APT values promoting secondary aerosol
467 formation (Huang et al., 2014; Quan et al., 2015; Ding et al., 2021); (iii) more influence from
468 natural emissions in the form of dust (especially JJA) and sea salt (especially SON) (Aldhaif et al.,
469 2021). Another noteworthy result is that the season with the clearest scavenging signature (DJF)
470 shows the most sensitivity (i.e., steepest downward slope) between the first two APT bins (0.9 mm
471 versus 4.3 mm) as there was a 26% reduction in $PM_{2.5}/\Delta CO$ ($0.584 \mu\text{g m}^{-3} \text{ppbv}^{-1}$ to $0.435 \mu\text{g m}^{-3}$
472 ppbv^{-1}), resulting in a slope (units of $\mu\text{g m}^{-3} \text{ppbv}^{-1} \text{mm}^{-1}$) of -0.044 in contrast to slopes of -0.007
473 and -0.006 for the subsequent two pairs of bins in DJF.



474 **Figure 7. Seasonal sensitivity of $PM_{2.5}/\Delta CO$ to APT for Cluster 1 trajectories, divided based**
475 **on four APT bins that have a similar number of data points per season. Markers denote**
476 **median values and error bars represent the 95% confidence interval for medians based on a**
477 **bootstrapping method ($n = 100,000$). Number of points per marker: DJF = 192 – 194; MAM**
478 **= 247 – 251; JJA = 107 – 110; SON = 183 – 191.**
479

480
481 We next address some additional details motivated by values shown in Table 2. We
482 examine three aerosol constituents linked to anthropogenic outflow from North America, including
483 sulfate, black carbon (BC), and organic carbon (OC) from MERRA-2 reanalysis. We recognize
484 that sulfate and OC have non-anthropogenic precursor vapors such as ocean-emitted dimethyl
485 sulfide and biogenic volatile organic compounds, respectively. Being the most abundant of the
486 three, sulfate exhibits the same characteristics as $PM_{2.5}$ when normalized by ΔCO with the sharpest
487 reduction at high APT conditions in DJF, followed by MAM, and then finally by JJA and SON



488 albeit with p -values > 0.05 for the latter two seasons as compared to low APT conditions. $BC/\Delta CO$
489 ratios show the same relative characteristics between APT categories as sulfate/ ΔCO for each
490 season, and mostly the same for $OC/\Delta CO$ except that the reduction in the median value in high
491 APT conditions for SON was significant (p -value < 0.05). Regardless of season, but most
492 pronounced in DJF, was the consistent result that $OC/\Delta CO$ exhibited the highest relative reduction
493 at high APT conditions (versus low APT) compared to BC and sulfate. Further work with more
494 expansive observational data is needed to better understand how different species respond to wet
495 scavenging.

496 Normalization by ΔCO was important for assessing transport efficiency of anthropogenic
497 pollution, but we also considered dust and sea salt without ΔCO normalization as they are
498 predominantly emitted by natural sources. Although outside the scope of this study, we caution
499 that MERRA-2 concentrations of sea salt in the $PM_{2.5}$ fraction may exceed those of total $PM_{2.5}$ as
500 measured at Ft. Prospect (Table 2) owing to the inherent differences in the two respective datasets
501 including the larger spatial scale covered by MERRA-2 as compared to the point measurements at
502 Ft. Prospect. Previous analysis of precipitation scavenging ratios over Bermuda showed that larger
503 aerosol types (e.g., sea salt) are removed more efficiently than smaller aerosol types (e.g., sulfate,
504 nitrate) (Galloway et al., 1993). Total sea salt and sea salt in the $PM_{2.5}$ fraction exhibited higher
505 median concentrations for the high APT category (p -value < 0.05) for all seasons except JJA,
506 which had more comparable values. This can be explained by how the high APT days exhibited
507 significantly higher surface wind speeds around Bermuda for all seasons except JJA, for which
508 wind speeds in general were depressed. Therefore, the reduction of the $PM_{2.5}/\Delta CO$ ratio in high
509 APT conditions may actually be an underestimate of wet scavenging of North American pollution
510 outflow since local sea salt is higher windier days marked by high APT.

511 To put this last assertion on firmer ground, we examined local rain values as they could be
512 influential in terms of scavenging the locally generated sea salt. The median values of local rain
513 on high APT days for each season based on APT for the most recent 6 hours of trajectories arriving
514 at Bermuda (APT_{6h}) were 0.0 – 0.1 mm, while median values of APT_{6h} on low APT days were 0
515 mm in each season. The only significant difference in median APT_{6h} values was in DJF when it
516 was 0.1 mm on high APT days in contrast to 0.0 mm on low APT days. Therefore, for DJF the
517 slightly enhanced APT_{6h} can possibly offset the greater sea salt emissions in terms of impacting
518 $PM_{2.5}$ levels over Bermuda. Results for the other major natural aerosol type (dust) reveal much
519 lower overall concentrations as compared to sea salt for both bulk sizes and the $PM_{2.5}$ fraction.
520 There was no consistent trend across the four seasons in terms of dust levels being higher for either
521 the low or high APT category, which is not unexpected as dust is not a major aerosol type expected
522 from North American outflow (Yu et al., 2020; Corral et al., 2021).

523 524 3.3.1 Volume Size Distributions

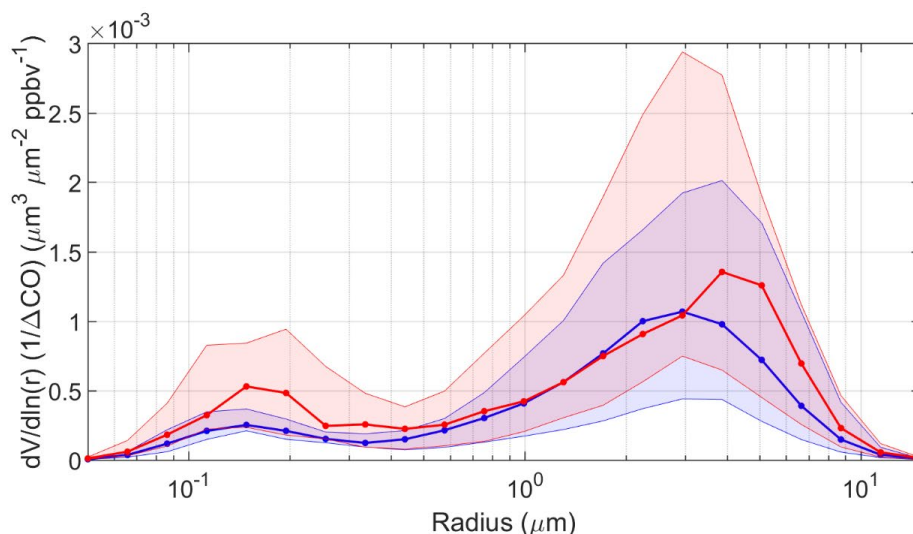
525 We next examine AERONET volume size distribution (VSD) relationships with APT. We
526 normalize the volume concentration data by corresponding ΔCO in the same way as was done for
527 $PM_{2.5}$, with the same condition of using data only when $\Delta CO > 3.2$ ppbv. A few cautionary details
528 are first noted about these data in comparison to APT: (i) there are limited VSD data in the
529 AERONET dataset, which is why we use all seasons of data together for Fig. 8 and Table 2; (ii)
530 AERONET data are representative of ambient conditions and changes in relative humidity can
531 influence VSD profiles; and (iii) AERONET data are column-based and not necessarily
532 representative of only the surface layer where the trajectories end in our analysis of HYSPLIT
533 data. Related to the last point, past work noted that column optical properties over Bermuda can



534 be weakly correlated with such measurements at the surface (Aryal et al., 2014) due largely to
535 aerosol layers aloft (Ennis and Sievering, 1990). At the same time, studies have shown that there
536 can be enhanced number and volume concentrations in the marine boundary layer versus the free
537 troposphere over Bermuda (Horvath et al., 1990; Kim et al., 1990).

538 The median VSDs for both APT categories exhibit a bimodal profile with a more dominant
539 coarse mode, consistent with what is already known for Bermuda based on AERONET data
540 (Aldhaif et al., 2021). The unique aspect of this work is that in high APT conditions, there is a
541 reduction in median volume concentration in the smaller mode between radii of 0.05 and ~ 1 μm ,
542 with a slight enhancement on the leading shoulder of the larger mode between radii of 1.71 and
543 2.94 μm (Fig. 8). The greatest relative reductions in the fine mode, which is more indicative of
544 transported continental pollution, occurred between midpoint radii of 0.15 and 0.33 μm with
545 relative reductions in those four bins (i.e., midpoint radii = 0.15, 0.19, 0.26, and 0.33 μm) ranging
546 from 38% to 52%. The coarse mode peaked at larger radii (3.86 μm) in low APT conditions relative
547 to high APT conditions (2.94 μm).

548 Table 2 reports VSD parameter values for the APT categories separated by fine and coarse
549 modes. Although only significantly different based on 90% confidence (p-value = 0.09), the fine
550 mode volume concentration normalized by ΔCO in the high APT category was less than half (45%)
551 the value in the low APT category. There were insignificant differences between effective radii
552 and volume median radii, in addition to the geometric standard deviation for the fine mode between
553 APT categories. For the coarse mode, only the geometric standard deviation exhibited a significant
554 difference by being higher in the high APT category (0.684 versus 0.647), although we presume
555 that has less to do with actual scavenging effects and more to do with different times of the year
556 where the relative abundance of different coarse particle type changes.



557 **Figure 8. Volume size distributions (VSD) normalized by ΔCO for high APT (> 13 mm; blue, $n = 16$) and low APT (< 0.9 mm; red, $n = 19$) groups for Cluster 1 trajectories. Thick curves**
558 **correspond to medians and shaded areas extend to the 25th and 75th percentiles. VSDs are**
559 **based on AERONET data between 1 January 2015 and 31 December 2019.**
560
561
562

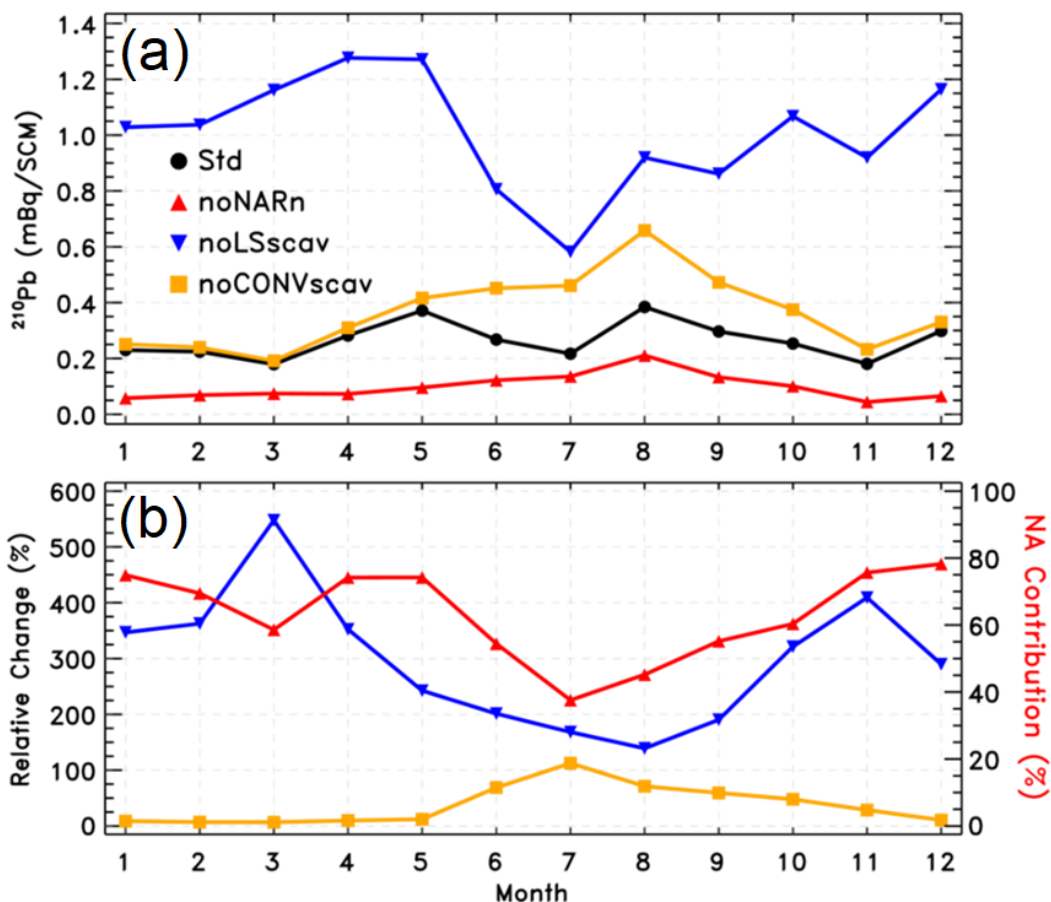


563 The AERONET results support the idea that scavenging on high APT days efficiently
564 removes fine particulate matter but that there can still be appreciable levels of locally generated
565 sea salt due to higher local surface winds on high APT days. Related to the columnar nature of
566 AERONET data, it is important to note that others have reported large-scale subsidence of
567 pollution from the mid and upper troposphere, especially in spring, based on enhanced ozone
568 mixing ratios at the surface of Bermuda (Oltmans and Levy, 1992; Cooper et al., 1998; Milne
569 et al., 2000; Li et al., 2002). Moreover, this phenomenon is synoptically favorable with the transport
570 of North American polluted air behind cold fronts especially in spring (Moody et al., 1995) and
571 often linked to the lifting of polluted air out of the boundary layer by convection over the
572 continental U.S. (Prados et al., 1999). It is unclear based on the current dataset how effective these
573 events were in impacting either the surface layer or columnar-based aerosol measurements at
574 Bermuda.

575

576 **3.4 GEOS-Chem Model Results**

577 We conduct four GEOS-Chem simulations of the ^{210}Pb submicron aerosol tracer including
578 a) one standard simulation; b) same as the standard simulation but with the ^{222}Rn tracer emissions
579 from the North American continent (25-60°N, 130-70°W) removed; c) same as the standard
580 simulation but without ^{210}Pb scavenging due to large-scale precipitation; and d) same as the
581 standard simulation but without ^{210}Pb scavenging by convective precipitation. The difference
582 between a) and b) quantifies the North American contribution to atmospheric ^{210}Pb concentrations.
583 The difference between a) and c) reflects the role of large-scale precipitation scavenging, while
584 the difference between a) and d) reflects that of convective precipitation scavenging in determining
585 atmospheric ^{210}Pb concentrations. All model simulations are conducted for the period from
586 September 2016 to December 2017 with the first four months for spin-up. Monthly mean outputs
587 for 2017 are used for analysis, which is a representative year within the time frame of the analysis
588 presented in Sections 3.1-3.3.



589
 590 **Figure 9. Simulated monthly surface ^{210}Pb tracer concentrations submicron mBq/SCM at**
 591 **Bermuda (32.31° N, 64.75° W) in 2017 as a way to assess effects of precipitation scavenging**
 592 **on North American outflow. Panel (a): monthly mean surface ^{210}Pb concentrations in the**
 593 **standard simulation ("Std") and three sensitivity simulations, i.e., without North**
 594 **American ^{222}Rn emissions ("noNARn"), without large-scale precipitation scavenging**
 595 **("noLSscav"), and without convective precipitation scavenging ("noCONVscav"). Panel (b):**
 596 **percentage changes, i.e., (noLSscav-Std)/Std \times 100 in blue and (noCONVscav-Std)/Std \times 100 in**
 597 **orange, and the North American contribution in red, i.e., (Std-noNARn)/Std \times 100.**
 598

599 Figure 9a shows monthly mean surface ^{210}Pb concentrations at Bermuda for 2017 in
 600 the standard simulation and three sensitivity simulations. Figure 9b plots the relative changes in
 601 simulated ^{210}Pb concentrations due to the effects of large-scale or convective precipitation
 602 scavenging. Also included in Fig. 9b is the North American contribution. The standard model
 603 simulates a seasonality in ^{210}Pb concentrations with two distinct peaks in May and August (upper
 604 panel). The May peak is a result of increased transport from North America in combination with
 605 reduced scavenging. In contrast, the August peak results from long-range transport from other
 606 continents (e.g., North Africa, Europe) along the southern edge of the Bermuda High. The lows in



607 March and November are attributed to strong large-scale precipitation scavenging, and the low in
608 July is associated with enhanced convective precipitation scavenging. The sensitivity simulations
609 clearly show that the role of large-scale precipitation scavenging in affecting surface ^{210}Pb
610 concentrations at Bermuda is much larger in winter/spring than in summer, with a maximum in
611 March (lower panel), while convective scavenging also plays an important role in summer. The
612 relative contribution of North American ^{222}Rn emissions is largest in winter (~75-80%), suggesting
613 air masses reaching Bermuda often experience large-scale precipitation scavenging while
614 traveling from the North American continent during winter. These model results are thus
615 consistent with previous results shown already and put our conclusions on firmer ground.

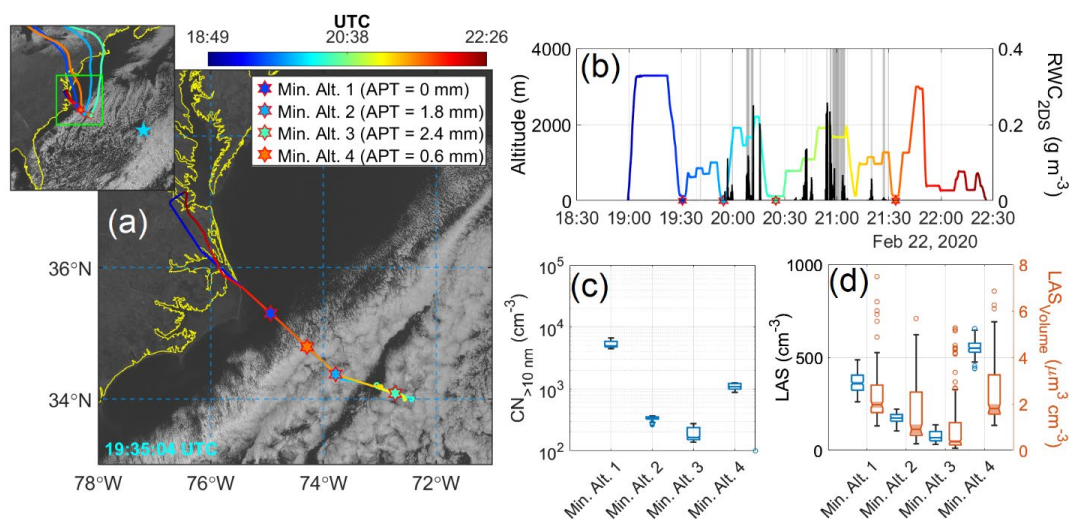
616

617 **3.5 Airborne Case Study**

618

619 The DJF season has been shown in this study to unite the greatest potential for wet
620 scavenging and the highest density of trajectories from North America reaching Bermuda. To
621 probe deeper now, we take advantage of data from ACTIVATE RF6 on 22 February 2020, which
622 characterized the intermediate region between North America and Bermuda. Weather in the
623 ACTIVATE domain on this day was characterized by a transition from post-cold front conditions
624 to high pressure. A cold front passed over Bermuda the previous day at approximately 18:00 UTC
625 on 21 February, and by the flight period of RF06 was approximately 600 km southeast of the
626 island. Meanwhile, a broad but weakening area of surface high pressure continued eastward into
627 the southeast U. S. Winds in the boundary layer were southwesterly at around 5 m s^{-1} near the base
628 of operations (NASA Langley Research Center; Hampton, Virginia), which were associated with
629 a weak trough on the northeast side of the high pressure system. These winds shifted to north-
630 northwest near the coast at 2.5 m s^{-1} and north-northeast at 7.4 m s^{-1} near the far end of the flight
631 track; Bermuda reported north-northeast winds around 9 m s^{-1} during this period. Aloft, 500 hPa
632 flow was from the west-northwest. NASA Langley reported few to no clouds during the flight
633 period, while Bermuda reported broken clouds with multiple layers (with bases around 900 m and
634 1800 m) and rain showers at or near the airport. This is consistent with satellite imagery (Fig. 10a),
635 which shows an area of scattered to broken cumulus and stratocumulus extending from the cold
636 front near Bermuda to the edge of the Gulf Stream off the U.S. East Coast. Satellite-retrieved cloud
637 bases were at 1–2 km, with cloud tops ranging from 1.5–3.5 km; from the HU-25 Falcon flight
638 legs, cloud bases encountered along the flight track were 750–1100 m and cloud tops were 1200–
639 1800 m.

639



640

641 **Figure 10. Summary of ACTIVATE's Research Flight 6 on 22 February 2020. (a) HU-25**
 642 **Falcon flight track overlaid on GOES-16 imagery with the smaller figure to the top left being**
 643 **a zoomed-out version of the WNAO (Bermuda denoted by blue star) and the larger figure**
 644 **zooming in on the area of the flight path. The midpoint of the four Min. Alt. legs are marked**
 645 **along with values for the accumulated precipitation along the trajectory (APT) for the recent**
 646 **history of the sampled air masses when they were over the ocean (time over land excluded**
 647 **from APT calculation). (b) Time series of Falcon altitude colored by flight UTC time (color**
 648 **bar in panel a) and rain water content (RWC) from the 2DS probe. Gray shaded bars signify**
 649 **when FCDP liquid water content exceeded 0.05 g m⁻³, indicative of cloud legs. The same four**
 650 **colored stars from (a) are shown on the x-axis to indicate where they occurred. (c-d) Box**
 651 **notch plots of the leg-mean Min. Alt. values of CPC particle (> 10 nm) concentration, and**
 652 **the number and volume concentrations of the LAS (> 0.09 μm).**

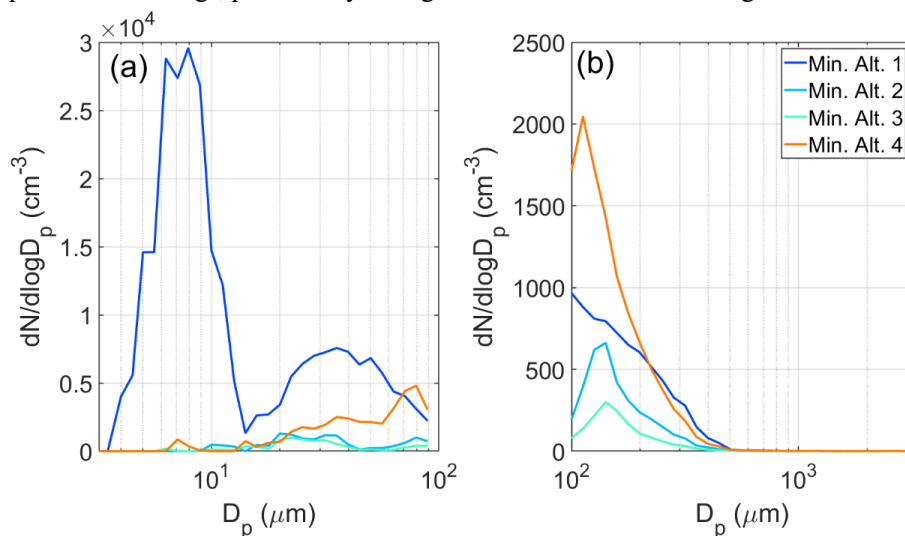
653

654 Figure 10a shows the general flight path, which involved flying to a point southeast of the
 655 operations base (Hampton, Virginia) and then re-tracing the path back to land. Four HYSPLIT
 656 back-trajectories are shown (Fig. 10a) corresponding to midpoints of each Min. Alt. leg when the
 657 aircraft was at its lowest altitude (~500 ft). APT calculations were conducted for segments of those
 658 four trajectories that were over the ocean. As a successful validation of the technique, no rain
 659 accumulated up to the point of the Min. Alt. 1 leg, as there were cloud-free conditions between
 660 land and that offshore point. In contrast, the next three Min. Alt. legs show higher APT values
 661 ranging from 0.6 to 2.4 mm, consistent with the GOES-16 imagery showing cloud fraction
 662 increasing just to the southeast of the Min. Alt. 1 leg. Expectedly, APT values progressively
 663 increased with offshore distance as a result of air masses being exposed to clouds for longer
 664 periods.

665 Shortly after the Min. Alt. 1 leg, the Falcon conducted two consecutive pairs of BCB and
 666 ACB legs (i.e., below cloud base followed by above cloud base), followed by a slant descent to
 667 the Min. Alt. 2 leg, where RWC values were enhanced (up to 0.02 g m⁻³ at 19:55:22 UTC) owing



668 to precipitation from overlying clouds. Very shortly thereafter, RWC reached as high as 0.11 g m^{-3}
669 3 (19:56:50 UTC) in the slant ascent profile passing through clouds. The APT value in Min. Alt. 2
670 leg was 1.8 mm. A significant reduction was observed in the aerosol number and volume
671 concentrations for the Min. Alt. 2 leg as compared to the Min. Alt. 1 leg (Figs. 10c-d). CPC (> 10
672 nm) concentrations dropped by 93% from a leg-median value of 4938 cm^{-3} during Min. Alt. 1 to
673 345 cm^{-3} during Min. Alt. 2, whereas the LAS number and volume ($> 100 \text{ nm}$) concentrations
674 dropped from 360 cm^{-3} to 174 cm^{-3} and from $2.0 \mu\text{m}^3 \text{ cm}^{-3}$ to $0.9 \mu\text{m}^3 \text{ cm}^{-3}$, respectively. Size
675 distribution data in those two legs show a significant reduction in particle concentration across the
676 full diameter range as measured by the SMPS and LAS (Fig. 11). A notable feature from the SMPS
677 was a pronounced peak between $3.5 - 14.1 \text{ nm}$ suggestive of nucleation, that was absent in
678 subsequent Min. Alt. legs, presumably owing to some combination of coagulation and scavenging.



679

680 **Figure 11. Aerosol size distribution comparison (a = SMPS, b = LAS) between the four HU-**
681 **25 Falcon Min. Alt. legs during ACTIVATE Research Flight 6, as shown in Fig. 10.**

682

683 The aircraft continued southeast after the Min. Alt. 2 leg and passed through more patches
684 of precipitation, leading to the highest APT value of 2.4 mm in the Min. Alt. 3 leg, where leg-
685 median values were as follows: CPC = 165 cm^{-3} , LAS number = 66 cm^{-3} , LAS volume = $0.4 \mu\text{m}^3$
686 cm^{-3} . While the SMPS distributions in the Min. Alt. 2 and 3 legs were very similar, the LAS size
687 distribution in the Min. Alt. 3 leg is shifted towards lower concentrations, especially below 400
688 nm. On the path back towards Virginia, the Falcon conducted one final Min. Alt. 4 leg right before
689 the boundary between cloudy and clear air, with the APT value being 0.6 mm. Between the Min.
690 Alt. 3 and 4 legs, again, significant RWC values were observed reaching as high as 0.26 g m^{-3} at
691 20:54:20 UTC. Aerosol concentration measurements increased relative to the Min. Alt. 2 and 3
692 legs (leg-median values): CPC = 1076 cm^{-3} , LAS number = 545 cm^{-3} , LAS volume = $1.8 \mu\text{m}^3 \text{ cm}^{-3}$.
693 It is difficult to compare results from the Min. Alt. 1 and 4 legs as ~ 2 hours had passed and there
694 were different conditions impacting the two respective sampled air masses. The size distributions
695 varied considerably for the Min. Alt. 4 leg as compared to the other three legs with increased



696 concentrations between 20-200 nm, presumably as a result of continued pollution outflow and
697 more photochemistry and aerosol growth processing as compared to earlier in the day.

698 To conclude, it is plausible based on the case flight data that the emerging presence of
699 clouds and precipitation led to the substantial reduction of aerosol particles with distance offshore
700 via wet scavenging processes. Further research is warranted with more extensive data to move
701 closer to showing causal relationships between precipitation and aerosol particles. For instance, a
702 few points of caution from RF6 are worth mentioning. First, the coastal trajectories in Fig. 10
703 corresponding to the different Min Alt. legs originated from varying places extending from the
704 Virginia coast up north towards Cape Cod, Massachusetts. Secondly, cloud dynamics and
705 boundary layer structure can vary offshore. Related to the latter, PBLH data obtained from
706 MERRA-2 along the flight track revealed that there were deeper boundary layers farther offshore,
707 but not sufficiently deeper to fully explain the reductions in aerosol concentration: Min. Alt.
708 1/2/3/4 = 1156/1728/1740/1530 m. Lastly, aerosol concentrations linked to continental outflow
709 naturally decrease anyways offshore, including in cloud-free conditions, owing to dilution during
710 transport.

711

712 **4. Conclusion**

713 This study examines the sensitivity of surface aerosol characteristics over a remote area of
714 the western North Atlantic Ocean (Bermuda) to precipitation along trajectories coming from North
715 America. Based on trajectory clustering with HYSPLIT data, two characteristic transport corridors
716 to Bermuda's surface layer (100 m AGL) were identified, with the focus being the one coming
717 from North America (Cluster 1). Seasonal analysis of HYSPLIT and Bermuda surface data showed
718 that JJA is distinct in terms of having transport from the southeast with the other seasons, especially
719 DJF, having more North American influence with higher concentrations of CO. Comparing Cluster
720 1 trajectories data between high (>13.5 mm) and low (<0.9 mm) APT, there was a clear signature
721 of wet scavenging effects by precipitation with more than a two-fold reduction in $PM_{2.5}/\Delta CO$ in
722 DJF ($0.29 \mu g m^{-3} ppbv^{-1}$ versus $0.62 \mu g m^{-3} ppbv^{-1}$), with the reduction being less severe for other
723 seasons. The greatest sensitivity of $PM_{2.5}/\Delta CO$ to APT was at the lowest values (up to ~ 5 mm;
724 slope of $-0.044 \mu g m^{-3} ppbv^{-1} mm^{-1}$), above which the descending slope of $PM_{2.5}/\Delta CO$ versus APT
725 was less steep.

726 Speciated data indicate that anthropogenic species such as sulfate, black carbon, and
727 organic carbon are reduced as a function of APT (much like $PM_{2.5}$). However, sea salt was not
728 necessarily reduced and at times could even be higher at Bermuda with high APT conditions,
729 which is attributed to higher local wind speeds and emissions at the surface on days simultaneous
730 with high APT trajectories. Analysis of AERONET volume size distribution data at Bermuda
731 confirms the substantial reduction of fine mode volume concentrations in contrast to less change
732 in the coarse mode on high APT days. GEOS-Chem simulations of the radionuclide aerosol tracer
733 ^{210}Pb confirm that North American influence at the surface of Bermuda is highest in DJF, with
734 those air masses significantly impacted by large-scale precipitation; furthermore, convective
735 scavenging is shown to play an important role in summer months. A research flight from
736 ACTIVATE on 22 February 2020 demonstrates a significant gradient in aerosol number and
737 volume concentrations offshore of North America as soon as trajectories start passing across
738 clouds, consistent with increasing APT away from the coast leading to increased aerosol particle
739 removal.

740 Our results have implications for other remote marine regions impacted by transport of
741 continental emissions. These results also highlight the important role of precipitation in modifying



742 aerosol levels, including potentially their vertical distribution (e.g., Luan and Jaeglé, 2013), along
743 continental outflow trajectories. We show that cloud and precipitation processes along trajectories
744 have significant impacts on resultant aerosol characteristics, suggesting that wet scavenging
745 processes in models require stronger constraints than other aerosol microphysical/chemical
746 processes to improve the forecasting of aerosol properties in marine atmospheres.
747
748
749



750 *Data Availability.*

751 Fort Prospect Station Aerosol/Gas Measurements:
752 <https://doi.org/10.6084/m9.figshare.13651454.v2>

753 AERONET: <https://aeronet.gsfc.nasa.gov/>

754 HYSPLIT: <https://www.ready.noaa.gov/HYSPLIT.php>

755 MERRA-2: <https://disc.gsfc.nasa.gov/>

756 GEOS-Chem Model: http://wiki.seas.harvard.edu/geos-chem/index.php/GEOS-Chem_v11-01

757 Section 3.5 ACTIVATE Airborne Data:
758 <https://doi.org/10.5067/SUBORBITAL/ACTIVATE/DATA001>

759 Section 3.5 airport weather data: <http://mesonet.agron.iastate.edu/ASOS/>

760 Section 3.5 ocean surface analysis charts and GFS 500 hPa analysis:
761 <https://www.ncei.noaa.gov/data/ncep-charts/access/>

762 Section 3.5 North America Analysis/Satellite composite:
763 https://www.wpc.ncep.noaa.gov/archives/web_pages/sfc/sfc_archive_maps.php

764 Section 3.5 Satellite imagery/products: [https://satcorps.larc.nasa.gov/cgi-](https://satcorps.larc.nasa.gov/cgi-bin/site/showdoc?docid=4&cmd=field-experiment-homepage&exp=ACTIVATE)
765 [bin/site/showdoc?docid=4&cmd=field-experiment-homepage&exp=ACTIVATE](https://satcorps.larc.nasa.gov/cgi-bin/site/showdoc?docid=4&cmd=field-experiment-homepage&exp=ACTIVATE)

766 *Author contributions.* HD and MA conducted the analysis. AS and HD prepared the manuscript.
767 HL and BZ performed GEOS-Chem model radionuclide simulations and output analysis. All
768 authors contributed by providing input and/or participating in airborne data collection.

769 *Competing interests.* The authors declare that they have no conflict of interest.

770 *Acknowledgments.* The work was funded by NASA grant 80NSSC19K0442 in support of
771 ACTIVATE, a NASA Earth Venture Suborbital-3 (EVS-3) investigation funded by NASA's Earth
772 Science Division and managed through the Earth System Science Pathfinder Program Office. HL
773 and BZ acknowledge support from NASA grant 80NSSC19K0389. The AERONET station in
774 Bermuda is maintained on behalf of NASA by the Bermuda Institute of Ocean Sciences at the
775 Tudor Hill Marine Atmospheric Observatory, which is currently supported by NSF award
776 1829686, and by previous such awards during the time period in this study. Gas chemistry and PM
777 data at Fort Prospect are from the Bermuda Air Quality Program, operated by BIOS with funding
778 from the Department of Environment and Natural Resources, Government of Bermuda. The
779 authors acknowledge the NOAA Air Resources Laboratory (ARL) for the provision of the
780 HYSPLIT transport and dispersion model and READY website (<http://ready.arl.noaa.gov>) used in
781 this work. The Pacific Northwest National Laboratory (PNNL) is operated for DOE by the Battelle
782 Memorial Institute under contract DE-AC05-76RLO1830. The NASA Center for Climate
783 Simulation (NCCS) provided supercomputing resources. The GEOS-Chem model is managed by
784 the Atmospheric Chemistry Modeling Group at Harvard University with support from NASA



785 ACMAP and MAP programs. GEOS-Chem input files were obtained from the GEOS-Chem Data
786 Portal enabled by Compute Canada.

787

788 **References**

789 Aldhaif, A. M., Lopez, D. H., Dadashazar, H., Painemal, D., Peters, A. J., and Sorooshian, A.:
790 An Aerosol Climatology and Implications for Clouds at a Remote Marine Site: Case Study Over
791 Bermuda, *Journal of Geophysical Research: Atmospheres*, 126, e2020JD034038,
792 <https://doi.org/10.1029/2020JD034038>, 2021.

793 Altieri, K. E., Hastings, M. G., Gobel, A. R., Peters, A. J., and Sigman, D. M.: Isotopic
794 composition of rainwater nitrate at Bermuda: The influence of air mass source and chemistry in
795 the marine boundary layer, *J Geophys Res-Atmos*, 118, 11304-11316, 2013.

796 Anderson, J. R., Buseck, P. R., Patterson, T. L., and Arimoto, R.: Characterization of the
797 Bermuda tropospheric aerosol by combined individual-particle and bulk-aerosol analysis, *Atmos*
798 *Environ*, 30, 319-338, 1996.

799 Arimoto, R., Duce, R. A., Savoie, D. L., and Prospero, J. M.: Trace-Elements in Aerosol-
800 Particles from Bermuda and Barbados - Concentrations, Sources and Relationships to Aerosol
801 Sulfate, *J Atmos Chem*, 14, 439-457, 1992.

802 Arimoto, R., Duce, R. A., Ray, B. J., Ellis, W. G., Cullen, J. D., and Merrill, J. T.: Trace-
803 Elements in the Atmosphere over the North-Atlantic, *J Geophys Res-Atmos*, 100, 1199-1213,
804 [10.1029/94jd02618](https://doi.org/10.1029/94jd02618), 1995.

805 Arimoto, R., Snow, J. A., Graustein, W. C., Moody, J. L., Ray, B. J., Duce, R. A., Turekian, K.
806 K., and Maring, H. B.: Influences of atmospheric transport pathways on radionuclide activities in
807 aerosol particles from over the North Atlantic, *J Geophys Res-Atmos*, 104, 21301-21316, 1999.

808 Arimoto, R.: Eolian Dust and Climate: Relationships to Sources, Tropospheric Chemistry,
809 Transport and Deposition. *Earth-Science Reviews*, 54(1), 29-42, [https://doi.org/10.1016/S0012-](https://doi.org/10.1016/S0012-8252(01)00040-X)
810 [8252\(01\)00040-X](https://doi.org/10.1016/S0012-8252(01)00040-X), 2001.

811 Aryal, R. P., Voss, K. J., Terman, P. A., Keene, W. C., Moody, J. L., Welton, E. J., and Holben,
812 B. N.: Comparison of surface and column measurements of aerosol scattering properties over the
813 western North Atlantic Ocean at Bermuda, *Atmos Chem Phys*, 14, 7617-7629, 2014.

814 Bey, I., Jacob, D. J., Yantosca, R. M., Logan, J. A., Field, B. D., Fiore, A. M., Li, Q. B., Liu, H.,
815 Mickley, L. J. and Schultz, M. G.: Global modeling of tropospheric chemistry with assimilated
816 meteorology: Model description and evaluation, *J. Geophys. Res. Atmos.*, 106(D19), 23073–
817 23095, [doi:10.1029/2001JD000807](https://doi.org/10.1029/2001JD000807), 2001.

818 Brattich, E., Liu, H., Tositti, L., Considine, D. B., and Crawford, J. H.: Processes controlling the
819 seasonal variations in ^{210}Pb and ^7Be at the Mt. Cimone WMO-GAW global station, Italy: a
820 model analysis, *Atmos. Chem. Phys.*, 17(2), 1061-1080, [doi:10.5194/acp-17-1061-2017](https://doi.org/10.5194/acp-17-1061-2017), 2017.



- 821 Chen, L. Q., and Duce, R. A.: The Sources of Sulfate, Vanadium and Mineral Matter in Aerosol-
822 Particles over Bermuda, *Atmos Environ*, 17, 2055-2064, 1983.
- 823 Cooper, O. R., Moody, J. L., Davenport, J. C., Oltmans, S. J., Johnson, B. J., Chen, X., Shepson,
824 P. B., and Merrill, J. T.: Influence of springtime weather systems on vertical ozone distributions
825 over three North American sites, *J Geophys Res-Atmos*, 103, 22001-22013, 1998.
- 826 Corral, A. F., Braun, R. A., Cairns, B., Gorrooh, V. A., Liu, H., Ma, L., Mardi, A. H., Painemal,
827 D., Starnes, S., van Dierenhoven, B., Wang, H., Yang, Y., Zhang, B., and Sorooshian, A.: An
828 Overview of Atmospheric Features Over the Western North Atlantic Ocean and North American
829 East Coast – Part 1: Analysis of Aerosols, Gases, and Wet Deposition Chemistry, *Journal of*
830 *Geophysical Research: Atmospheres*, 126, e2020JD032592,
831 <https://doi.org/10.1029/2020JD032592>, 2021.
- 832 Cutter, G. A.: Metalloids in Wet Deposition on Bermuda - Concentrations, Sources, and Fluxes,
833 *J Geophys Res-Atmos*, 98, 16777-16786, 1993.
- 834 Dadashazar, H., Painemal, D., Alipanah, M., Brunke, M., Chellappan, S., Corral, A. F., Crosbie,
835 E., Kirschler, S., Liu, H., Moore, R., Robinson, C., Scarino, A. J., Shook, M., Sinclair, K.,
836 Thornhill, K. L., Voigt, C., Wang, H., Winstead, E., Zeng, X., Ziemba, L., Zuidema, P., and
837 Sorooshian, A.: Cloud Drop Number Concentrations over the Western North Atlantic Ocean:
838 Seasonal Cycle, Aerosol Interrelationships, and Other Influential Factors, *Atmos. Chem. Phys.*
839 *Discuss.*, 2021, 1-36, 10.5194/acp-2021-153, 2021.
- 840 Davis, R. E., Hayden, B. P., Gay, D. A., Phillips, W. L., and Jones, G. V.: The North Atlantic
841 Subtropical Anticyclone, *J Climate*, 10, 728-744, 10.1175/1520-
842 0442(1997)010<0728:tmsa>2.0.co;2, 1997.
- 843 Dimitriou, K., Remoundaki, E., Mantas, E., Kassomenos, P.: Spatial distribution of source areas
844 of PM_{2.5} by Concentration Weighted Trajectory (CWT) model applied in PM_{2.5} concentration
845 and composition data, *Atmospheric Environment* 116, 138–145,
846 doi:10.1016/j.atmosenv.2015.06.021, 2015.
- 847 Ding, J., Dai, Q., Zhang, Y., Xu, J., Huangfu, Y., Feng, Y.: Air humidity affects secondary
848 aerosol formation in different pathways, *Science of The Total Environment* 759, 143540,
849 doi:10.1016/j.scitotenv.2020.143540, 2021.
850
- 851 Dubovik, O., Holben, B., Eck, T. F., Smirnov, A., Kaufman, Y. J., King, M. D., Tanré, D., and
852 Slutsker, I.: Variability of Absorption and Optical Properties of Key Aerosol Types Observed in
853 Worldwide Locations, *J Atmos Sci*, 59, 590-608, 10.1175/1520-
854 0469(2002)059<0590:VOAAOP>2.0.CO;2, 2002.
- 855 Eastham, S. D., Weisenstein, D. K. and Barrett, S. R. H.: Development and evaluation of the
856 unified tropospheric-stratospheric chemistry extension (UCX) for the global chemistry-transport
857 model GEOS-Chem, *Atmos. Environ.*, 89, 52–63, doi:10.1016/j.atmosenv.2014.02.001, 2014.
- 858 Ennis, G., and Sievering, H.: Vertical Profile of Elemental Concentrations in Aerosol Particles in
859 the Bermuda Area during Gce/Case/Watox, *Global Biogeochem Cy*, 4, 179-188, 1990.



- 860 Galloway, J. N., Tokos, J. J., Knap, A. H., and Keene, W. C.: Local influences on the
861 composition of precipitation on Bermuda, *Tellus B: Chemical and Physical Meteorology*, 40,
862 178-188, 10.3402/tellusb.v40i3.15905, 1988.
- 863 Galloway, J. N., Keene, W. C., Artz, R. S., Miller, J. M., Church, T. M., and Knap, A. H.:
864 Processes controlling the concentrations of SO₄(=), NO₃(-), NH₄(+), H(+), HCOO(T) and
865 CH₃COO(T) in precipitation on Bermuda, *Tellus B*, 41, 427-443, 1989.
- 866 Galloway, J. N., Savoie, D. L., Keene, W. C., and Prospero, J. M.: The Temporal and Spatial
867 Variability of Scavenging Ratios for Nss Sulfate, Nitrate, Methanesulfonate and Sodium in the
868 Atmosphere over the North-Atlantic Ocean, *Atmos Environ a-Gen*, 27, 235-250, 1993.
- 869 Garrett, T., Zhao, C., Novelli, P.: Assessing the relative contributions of transport efficiency and
870 scavenging to seasonal variability in Arctic aerosol. *Tellus B: Chemical and Physical*
871 *Meteorology* 62, 190–196, doi:10.1111/j.1600-0889.2010.00453.x, 2010.
- 872 Gelaro, R., McCarty, W., Suarez, M. J., Todling, R., Molod, A., Takacs, L., Randles, C. A.,
873 Darmenov, A., Bosilovich, M. G., Reichle, R., Wargan, K., Coy, L., Cullather, R., Draper, C.,
874 Akella, S., Buchard, V., Conaty, A., da Silva, A. M., Gu, W., Kim, G. K., Koster, R., Lucchesi,
875 R., Merkova, D., Nielsen, J. E., Partyka, G., Pawson, S., Putman, W., Rienecker, M., Schubert,
876 S. D., Sienkiewicz, M., and Zhao, B.: The Modern-Era Retrospective Analysis for Research and
877 Applications, Version 2 (MERRA-2), *J Climate*, 30, 5419-5454, 10.1175/Jcli-D-16-0758.1, 891
878 2017.
- 879 Giles, D. M., Sinyuk, A., Sorokin, M. G., Schafer, J. S., Smirnov, A., Slutsker, I., Eck, T. F.,
880 Holben, B. N., Lewis, J. R., Campbell, J. R., Welton, E. J., Korkin, S. V., and Lyapustin, A. I.:
881 Advancements in the Aerosol Robotic Network (AERONET) Version 3 database – automated
882 near-real-time quality control algorithm with improved cloud screening for Sun photometer
883 aerosol optical depth (AOD) measurements, *Atmos. Meas. Tech.*, 12, 169-209, 10.5194/amt-12-
884 169-2019, 2019.
- 885 Govender, P. and Sivakumar, V.: Application of k-means and hierarchical clustering techniques
886 for analysis of air pollution: A review (1980–2019), *Atmospheric Pollution Research*, 11, 40–56,
887 <https://doi.org/10.1016/j.apr.2019.09.009>, 2020.
- 888 Government of Bermuda: 2016 Population and Housing Census Report. Retrieved from
889 <https://www.gov.bm/articles/2016-population-and-housing-census-report>, 2019.
- 890 Hilario, M. R. A., Cruz, M. T., Bañaga, P. A., Betito, G., Braun, R. A., Stahl, C., Cambaliza, M.
891 O., Lorenzo, G. R., MacDonald, A. B., AzadiAghdam, M., Pabroa, P. C., Yee, J. R., Simpas, J.
892 B., and Sorooshian, A.: Characterizing Weekly Cycles of Particulate Matter in a Coastal
893 Megacity: The Importance of a Seasonal, Size-Resolved, and Chemically Speciated Analysis,
894 *Journal of Geophysical Research: Atmospheres*, 125, e2020JD032614,
895 <https://doi.org/10.1029/2020JD032614>, 2020.
- 896 Hilario, M. R. A., Crosbie, E., Shook, M., Reid, J. S., Cambaliza, M. O. L., Simpas, J. B. B.,
897 Ziemba, L., DiGangi, J. P., Diskin, G. S., Nguyen, P., Turk, F. J., Winstead, E., Robinson, C. E.,



- 898 Wang, J., Zhang, J., Wang, Y., Yoon, S., Flynn, J., Alvarez, S. L., Behrangi, A., and Sorooshian,
899 A.: Measurement report: Long-range transport patterns into the tropical northwest Pacific during
900 the CAMP2Ex aircraft campaign: chemical composition, size distributions, and the impact of
901 convection, *Atmos. Chem. Phys.*, 21, 3777-3802, 10.5194/acp-21-3777-2021, 2021.
- 902 Holben, B. N., Eck, T. F., Slutsker, I., Tanré, D., Buis, J. P., Setzer, A., Vermote, E., Reagan, J.
903 A., Kaufman, Y. J., Nakajima, T., Lavenu, F., Jankowiak, I., and Smirnov, A.: AERONET—A
904 Federated Instrument Network and Data Archive for Aerosol Characterization, *Remote Sens
905 Environ*, 66, 1-16, [https://doi.org/10.1016/S0034-4257\(98\)00031-5](https://doi.org/10.1016/S0034-4257(98)00031-5), 1998.
- 906 Horvath, H., Gunter, R. L., and Wilkison, S. W.: Determination of the Coarse Mode of the
907 Atmospheric Aerosol Using Data from a Forward-Scattering Spectrometer Probe, *Aerosol Sci
908 Tech*, 12, 964-980, 10.1080/02786829008959407, 1990.
- 909 Hsu, Y.-K., Holsen, T.M., Hopke, P.K.: Comparison of hybrid receptor models to locate PCB
910 sources in Chicago. *Atmospheric Environment* 37, 545–562, doi:10.1016/s1352-2310(02)00886-
911 5, 2003.
- 912 Huang, R.-J., Zhang, Y., Bozzetti, C., Ho, K.-F., Cao, J.-J., Han, Y., Daellenbach, K.R., Slowik,
913 J.G., Platt, S.M., Canonaco, F., Zotter, P., Wolf, R., Pieber, S.M., Bruns, E.A., Crippa, M.,
914 Ciarelli, G., Piazzalunga, A., Schwikowski, M., Abbaszade, G., Schnelle-Kreis, J., Zimmermann,
915 R., An, Z., Szidat, S., Baltensperger, U., Haddad, I.E., Prévôt, A.S.H.: High secondary aerosol
916 contribution to particulate pollution during haze events in China. *Nature* 514, 218–222,
917 doi:10.1038/nature13774, 2014.
- 918 Huang, S. L., Rahn, K. A., Arimoto, R., Graustein, W. C., and Turekian, K. K.: Semiannual
919 cycles of pollution at Bermuda, *J Geophys Res-Atmos*, 104, 30309-30317, 1999.
- 920 Jickells, T. D., Knap, A., Church, T., Galloway, J., and Miller, J.: Acid-Rain on Bermuda,
921 *Nature*, 297, 55-57, 1982.
- 922 Kadko, D., and Prospero, J.: Deposition of Be-7 to Bermuda and the regional ocean:
923 Environmental factors affecting estimates of atmospheric flux to the ocean, *J Geophys Res-
924 Oceans*, 116, 2011.
- 925 Kassomenos, P., Vardoulakis, S., Borge, R., Lumberras, J., Papaloukas, C., Karakitsios, S.:
926 Comparison of statistical clustering techniques for the classification of modelled atmospheric
927 trajectories. *Theoretical and Applied Climatology* 102, 1–12, doi:10.1007/s00704-009-0233-7,
928 2010.
- 929 Keene, W. C., Moody, J. L., Galloway, J. N., Prospero, J. M., Cooper, O. R., Eckhardt, S., and
930 Maben, J. R.: Long-term trends in aerosol and precipitation composition over the western North
931 Atlantic Ocean at Bermuda, *Atmos Chem Phys*, 14, 8119-8135, 2014.
- 932 Kim, Y., Sievering, H., and Boatman, J.: Volume and surface area size distribution, water mass
933 and model fitting of GCE/CASE/WATOX marine aerosols, *Global Biogeochem Cy*, 4, 165-177,
934 <https://doi.org/10.1029/GB004i002p00165>, 1990.



- 935 Knop, I., Bansmer, S.E., Hahn, V., Voigt, C.: Comparison of different droplet measurement
936 techniques in the Braunschweig Icing Wind Tunnel. *Atmospheric Measurement Techniques* 14,
937 1761–1781, doi:10.5194/amt-14-1761-2021, 2021.
- 938 Lawson, R.P., O'Connor, D., Zmarzly, P., Weaver, K., Baker, B., Mo, Q., Jonsson, H.: The 2D-S
939 (Stereo) Probe: Design and Preliminary Tests of a New Airborne, High-Speed, High-Resolution
940 Particle Imaging Probe. *Journal of Atmospheric and Oceanic Technology* 23, 1462–1477,
941 doi:10.1175/jtech1927.1, 2006.
- 942 Li, Q., Jacob, D. J., Fairlie, T. D., Liu, H., Martin, R. V., and Yantosca, R. M.: Stratospheric
943 versus pollution influences on ozone at Bermuda: Reconciling past analyses, *J. Geophys. Res.*,
944 107, 4611, doi:10.1029/2002JD002138, 2002.
- 945
946 Lin, J. T., and McElroy, M. B.: Impacts of boundary layer mixing on pollutant vertical profiles in
947 the lower troposphere: Implications to satellite remote sensing, *Atmos. Environ.*, 44(14), 1726–
948 1739, doi:10.1016/j.atmosenv.2010.02.009, 2010.
- 949 Lin, S.-J., and Rood, R. B.: Multidimensional Flux-Form Semi-Lagrangian Transport Schemes,
950 *Mon Weather Rev*, 124, 2046–2070, 10.1175/1520-0493(1996)124<2046:MFFSLT>2.0.CO;2,
951 1996.
- 952 Liu, H., Jacob, D. J., Bey, I. and Yantosca, R. M.: Constraints from ^{210}Pb and ^7Be on wet
953 deposition and transport in a global three-dimensional chemical tracer model driven by
954 assimilated meteorological fields, *J. Geophys. Res. Atmos.*, 106(D11), 12109–12128,
955 doi:10.1029/2000JD900839, 2001.
- 956 Luan, Y., Jaeglé, L.: Composite study of aerosol export events from East Asia and North
957 America, *Atmospheric Chemistry and Physics* 13, 1221–1242, doi:10.5194/acp-13-1221-2013,
958 2013.
- 959 Luo, G., Yu, F., and Schwab, J.: Revised treatment of wet scavenging processes dramatically
960 improves GEOS-Chem 12.0.0 simulations of surface nitric acid, nitrate, and ammonium over the
961 United States, *Geosci. Model Dev.*, 12, 3439–3447, <https://doi.org/10.5194/gmd-12-3439-2019>,
962 2019.
- 963 Matsui, H., Kondo, Y., Moteki, N., Takegawa, N., Sahu, L.K., Zhao, Y., Fuelberg, H.E.,
964 Sessions, W.R., Diskin, G., Blake, D.R., Wisthaler, A., Koike, M.: Seasonal variation of the
965 transport of black carbon aerosol from the Asian continent to the Arctic during the ARCTAS
966 aircraft campaign, *Journal of Geophysical Research: Atmospheres* 116,
967 doi:10.1029/2010jd015067, 2011.
- 968 Mead, C., Herckes, P., Majestic, B. J., and Anbar, A. D.: Source apportionment of aerosol iron in
969 the marine environment using iron isotope analysis, *Geophys Res Lett*, 40, 5722–5727, 2013.
- 970 Merrill, J. T.: Isentropic Air-Flow Probability Analysis, *J Geophys Res-Atmos*, 99, 25881-
971 25889, 1994.



- 972 Miller, J. M., and Harris, J. M.: The Flow Climatology to Bermuda and Its Implications for
973 Long-Range Transport, *Atmos Environ*, 19, 409-414, 1985.
- 974 Milne, P. J., Prados, A. I., Dickerson, R. R., Doddridge, B. G., Riemer, D. D., Zika, R. G.,
975 Merrill, J. T., and Moody, J. L.: Nonmethane hydrocarbon mixing ratios in continental outflow
976 air from eastern North America: Export of ozone precursors to Bermuda, *J Geophys Res-Atmos*,
977 105, 9981-9990, 2000.
- 978 Moody, J. L., and Galloway, J. N.: Quantifying the relationship between atmospheric transport
979 and the chemical composition of precipitation on Bermuda, *Tellus B: Chemical and Physical*
980 *Meteorology*, 40, 463-479, 10.3402/tellusb.v40i5.16014, 1988.
- 981 Moody, J. L., Oltmans, S. J., Levy II, H., and Merrill, J. T.: A transport climatology of
982 tropospheric ozone, Bermuda: 1988–1991, *J. Geophys. Res.*, 100, 7179-7194, 1995.
- 983 Moody, J. L., Keene, W. C., Cooper, O. R., Voss, K. J., Aryal, R., Eckhardt, S., Holben, B.,
984 Maben, J. R., Izaguirre, M. A., and Galloway, J. N.: Flow climatology for physicochemical
985 properties of dichotomous aerosol over the western North Atlantic Ocean at Bermuda, *Atmos*
986 *Chem Phys*, 14, 691-717, 2014.
- 987 Moteki, N., Kondo, Y., Oshima, N., Takegawa, N., Koike, M., Kita, K., Matsui, H., and Kajino,
988 M.: Size dependence of wet removal of black carbon aerosols during transport from the
989 boundary layer to the free troposphere, *Geophys Res Lett*, 39,
990 <https://doi.org/10.1029/2012GL052034>, 2012.
- 991 Muhs, D. R., Budahn, J. R., Prospero, J. M., Skipp, G., & Herwitz, S. R.: Soil Genesis on the
992 Island of Bermuda in the Quaternary: The Importance of African Dust Transport and Deposition.
993 *Journal of Geophysical Research-Earth Surface*, 117, 2012.
- 994 Oltmans, S. J., and Levy, H.: Seasonal Cycle of Surface Ozone over the Western North-Atlantic,
995 *Nature*, 358, 392-394, 1992.
- 996 Oshima, N., Kondo, Y., Moteki, N., Takegawa, N., Koike, M., Kita, K., Matsui, H., Kajino, M.,
997 Nakamura, H., Jung, J. S., and Kim, Y. J.: Wet removal of black carbon in Asian outflow:
998 Aerosol Radiative Forcing in East Asia (A-FORCE) aircraft campaign, *Journal of Geophysical*
999 *Research: Atmospheres*, 117, <https://doi.org/10.1029/2011JD016552>, 2012.
- 1000 Painemal, D., Corral, A. F., Sorooshian, A., Brunke, M. A., Chellappan, S., Afzali Gorooh, V.,
1001 Ham, S.-H., O'Neill, L., Smith Jr, W. L., Tselioudis, G., Wang, H., Zeng, X., and Zuidema, P.:
1002 An Overview of Atmospheric Features Over the Western North Atlantic Ocean and North
1003 American East Coast—Part 2: Circulation, Boundary Layer, and Clouds, *Journal of Geophysical*
1004 *Research: Atmospheres*, 126, e2020JD033423, <https://doi.org/10.1029/2020JD033423>, 2021.
- 1005 Park, R.J., Jacob, D.J., Palmer, P.I., Clarke, A.D., Weber, R.J., Zondlo, M.A., Eisele, F.L.,
1006 Bandy, A.R., Thornton, D.C., Sachse, G.W., Bond, T.C: Export efficiency of black carbon
1007 aerosol in continental outflow: Global implications, *Journal of Geophysical Research:*
1008 *Atmospheres* 110, doi:10.1029/2004jd005432, 2005.



- 1009 Prados, A. I., Dickerson, R. R., Doddridge, B. G., Milne, P. A., Moody, J. L., and Merrill, J. T.:
1010 Transport of ozone and pollutants from North America to the North Atlantic Ocean during the
1011 1996 Atmosphere/Ocean Chemistry Experiment (AEROCE) intensive, *J Geophys Res-Atmos*,
1012 104, 26219-26233, 1999.
- 1013 Quan, J., Liu, Q., Li, X., Gao, Y., Jia, X., Sheng, J., Liu, Y.: Effect of heterogeneous aqueous
1014 reactions on the secondary formation of inorganic aerosols during haze events. *Atmospheric*
1015 *Environment* 122, 306–312, doi:10.1016/j.atmosenv.2015.09.068, 2015.
- 1016 Rolph, G., Stein, A., Stunder, B.: Real-time Environmental Applications and Display sYstem:
1017 READY, *Environmental Modelling & Software* 95, 210–228, doi:10.1016/j.envsoft.2017.06.025,
1018 2017.
- 1019 Schuster, G. L., Dubovik, O., and Holben, B. N.: Angstrom exponent and bimodal aerosol size
1020 distributions, *Journal of Geophysical Research: Atmospheres*, 111,
1021 <https://doi.org/10.1029/2005JD006328>, 2006.
- 1022 Silva, S. J., Ridley, D. A., and Heald, C. L.: Exploring the Constraints on Simulated Aerosol
1023 Sources and Transport Across the North Atlantic With Island-Based Sun Photometers, *Earth*
1024 *Space Sci*, 7, e2020EA001392, <https://doi.org/10.1029/2020EA001392>, 2020.
- 1025 Sinnott, R. W.: Virtues of the haversine, *Sky and Telescope*, Vol.68, No.2, p.159, 1984.
- 1026 Sorooshian, A., Anderson, B., Bauer, S. E., Braun, R. A., Cairns, B., Crosbie, E., . . . Zuidema,
1027 P.: Aerosol–Cloud–Meteorology Interaction Airborne Field Investigations: Using Lessons
1028 Learned from the U.S. West Coast in the Design of ACTIVATE Off the U.S. East Coast,
1029 *Bulletin of the American Meteorological Society*, 100(8), 1511-1528. doi:10.1175/bams-d-18-
1030 0100.1, 2019.
- 1031 Sorooshian, A., Corral, A. F., Braun, R. A., Cairns, B., Crosbie, E., Ferrare, R., . . . Zuidema, P.:
1032 Atmospheric Research over the Western North Atlantic Ocean Region and North American East
1033 Coast: A Review of Past Work and Challenges Ahead, *Journal of Geophysical Research:*
1034 *Atmospheres*, 125(6), <https://doi.org/10.1029/2019JD031626>, 2020.
- 1035 Stein, A.F., Draxler, R.R., Rolph, G.D., Stunder, B.J.B., Cohen, M.D., Ngan, F.: NOAA’s
1036 HYSPLIT Atmospheric Transport and Dispersion Modeling System. *Bulletin of the American*
1037 *Meteorological Society* 96, 2059–2077, doi:10.1175/bams-d-14-00110.1, 2015.
- 1038 Todd, D. L., Keene, W. C., Moody, J. L., Maring, H., and Galloway, J. N.: Effects of wet
1039 deposition on optical properties of the atmosphere over Bermuda and Barbados, *J Geophys Res-*
1040 *Atmos*, 108, 10.1029/2001jd001084, 2003.
- 1041 US-EPA: Compendium of Methods for the de-termination of inorganic compounds in
1042 ambient air, USEPA/625/R-96/010a, United States Environmental Protection Agency,
1043 Washington, D.C., 1999.



- 1044 Veron, A. J., Church, T. M., Patterson, C. C., Erel, Y., and Merrill, J. T.: Continental Origin and
1045 Industrial Sources of Trace-Metals in the Northwest Atlantic Troposphere, *J Atmos Chem*, 14,
1046 339-351, 1992.
- 1047 Wang, Q., Jacob, D. J., Fisher, J. A., Mao, J., Leibensperger, E. M., Carouge, C. C., Le Sager, P.,
1048 Kondo, Y., Jimenez, J. L., Cubison, M. J., Doherty, S. J., Sager, P. Le, Kondo, Y., Jimenez, J. L.,
1049 Cubison, M. J., and Doherty, S.J.: Sources of carbonaceous aerosols and deposited black carbon
1050 in the Arctic in winter-spring: implications for radiative forcing, *Atmos. Chem. Phys.*, 11(23),
1051 12453–12473, doi:10.5194/acp-11-12453-2011, 2011, 2011.
- 1052 Wang, Y.Q., Zhang, X.Y., Draxler, R.R.: TrajStat: GIS-based software that uses various
1053 trajectory statistical analysis methods to identify potential sources from long-term air pollution
1054 measurement data. *Environmental Modelling & Software* 24, 938–939,
1055 doi:10.1016/j.envsoft.2009.01.004, 2009.
- 1056 Weinstock, B.: Carbon Monoxide: Residence Time in the Atmosphere, 166, 224–225,
1057 <https://doi.org/10.1126/science.166.3902.224>, 1969.
- 1058 Wesely, M. L.: Parameterization of surface resistances to gaseous dry deposition in regional-
1059 scale numerical models, *Atmospheric Environment* (1967), 23, 1293-1304,
1060 [https://doi.org/10.1016/0004-6981\(89\)90153-4](https://doi.org/10.1016/0004-6981(89)90153-4), 1989.
- 1061 Wolff, G. T., Ruthkosky, M. S., Stroup, D. P., Korsog, P. E., Ferman, M. A., Wendel, G. J., and
1062 Stedman, D. H.: Measurements of SO_x, NO_x and Aerosol Species on Bermuda, *Atmos Environ*,
1063 20, 1229-1239, 1986.
- 1064 Wu, S., Mickley, L. J., Jacob, D. J., Logan, J. A., Yantosca, R. M. and Rind, D. Why are there
1065 large differences between models in global budgets of tropospheric ozone? *J. Geophys. Res.*
1066 *Atmos.*, 112(D5), 1–18, doi:10.1029/2006JD007801, 2007.
- 1067 Yu, H., Yang, Y., Wang, H., Tan, Q., Chin, M., Levy, R.C., Remer, L.A., Smith, S.J., Yuan, T.,
1068 Shi, Y.: Interannual variability and trends of combustion aerosol and dust in major continental
1069 outflows revealed by MODIS retrievals and CAM5 simulations during 2003–2017, *Atmospheric*
1070 *Chemistry and Physics* 20, 139–161, doi:10.5194/acp-20-139-2020, 2020.
- 1071 Yu, K., Keller, C. A., Jacob, D. J., Molod, A. M., Eastham, S. D. and Long, M. S.: Errors and
1072 improvements in the use of archived meteorological data for chemical transport modeling: an
1073 analysis using GEOS-Chem v11-01 driven by GEOS-5 meteorology, *Geosci. Model Dev.*, 11,
1074 305–319, doi:10.5194/gmd-2017-125, 2018.
- 1075 Zhang, B., Liu, H., Crawford, J. H., Chen, G., Fairlie, T. D., Chambers, S., Kang, C.-H.,
1076 Williams, A. G., Zhang, K., Considine, D. B., Sulprizio, M. P., and Yantosca, R. M.: Simulation
1077 of radon-222 with the GEOS-Chem global model: emissions, seasonality, and convective
1078 transport, *Atmos. Chem. Phys.*, 21, 1861–1887, <https://doi.org/10.5194/acp-21-1861-2021>, 2021.